Construction and Preparation of an Experimental Setup for Excitation and Detection of Rydberg Atoms in a Cryogenic Environment

Johanna Popp

Masterarbeit in Physik
angefertigt im Institut für Angewandte Physik

vorgelegt der
Mathematisch-Naturwissenschaftlichen Fakultät
der
Rheinischen Friedrich-Wilhelms-Universität
Bonn

April 2024

I hereby declare that this thesis was formulated by myself and that no sources or tools other than those cited were used.

Bonn, 02.04.2024 ....
Date Signature

1. Gutachter: Prof. Dr. Sebastian Hofferberth
2. Gutachter: Prof. Dr. Stefan Linden

Contents

CHAPTER 1

Introduction

Electromechanical oscillators are a promising option for quantum memory and transducers [1, 2], which can be employed in quantum information [3] and metrology [4]. This is due to the combination of high-quality factors that can go above 7×10^5 [4, 5] and long coherence times achieved at operation frequencies in the range between 6 - 10 GHz [5, 6], which also enables interfacing with superconducting qubits operating in the same frequency range [7]. Furthermore, electro-mechanical oscillators are large quantum systems and can used for fundamental research on the boundary between quantum mechanics and classical physics [8, 9].

For these applications, electro-mechanical oscillators need to be cooled to their motional ground state to reduce thermal noise [10] and to enable coherent operation [11]. Mechanical oscillators with modes in the GHz regime can be cooled directly to the quantum ground state using a mK dilution refrigerator [6]. However, where direct cooling to the mechanical ground state is not possible, for example, due to higher temperatures of the environment, additional heat sources or operation at lower resonance frequencies, additional cooling schemes such as sideband cooling [12] need to be employed.

In order to control, read out, or use the electro-mechanical oscillators for transduction between optical and microwave photons, they have been coupled to optical or microwave resonators, including Fabry-Perot resonators [13], photonic crystals [14] and superconducting qubits[15]. The experimental work for this thesis was carried out in one of Professor Hofferberth's experiments, which aims to couple a high overtone bulk acoustic resonator (a type of electro-mechanical oscillators [8]) to Rydberg atoms in a novel hybrid system.

Rydberg atoms are excellent candidates to create a hybrid system due to their properties. Their transition extends over a wide range of transition wavelengths, from the optical regime near the ground state to the microwave regime between neighbouring Rydberg states [16, 17]. The strong transition between the neighbouring Rydberg states makes them sensitive antennas for microwave fields [18].

The goal of this experiment in Bonn is to cool a vibrational mode of the electro-mechanical oscillator in the GHz regime to its motional groundstate. No dilution refrigerator is used in this process. Instead, a closed cycle cryostat will be used to cool the electro-mechanical oscillator to 4.2 K. This corresponds to a thermal occupation of $\bar{n}_{\text{thermal}} = 15$ at the target frequency of 5.8 GHz[1][19]. The remaining phonons are extracted using the interaction with the Rydberg atoms.

For that purpose rubidium atoms are trapped above the electro-mechanical oscillator by a magnetic

---

[1] The thermal occupation is calculated via: $\bar{n}_{\text{thermal}} = k_B T/(f \cdot h)$[19]

field, generated by a z-shaped wire fabricated on an atom-chip [20]. The rubidium atoms are excited to the Rydberg state with a two-photon excitation scheme, using highly focused laser beams at 780 nm and 480 nm wavelength. By changing the magnetic field, the distance between the Rydberg atoms and the electro-mechanical oscillator can be changed and so the coupling strength of the hybrid system can be controlled.

The cold rubidium atom cloud is prepared in a separate chamber from the science chamber. This is done to allow fast loading into a magneto-optical trap (MOT) from high-pressure background vapour without degrading the pressure in the science region or heating the cryogenic region with the MOT beams. The atoms will be transported from the preparation chamber to the science chamber with a magnetic transport [21].

The aim of this thesis was to extend and complete the setup for the cold atom preparation for the planned experiment. During this thesis, a homemade science chamber for the cryogenic setup was constructed and tested. The magnetic transport was assembled, and an intermediate room temperature setup was built for testing the cold atom preparation, including the transport of atoms into the science chamber.

Chapter 2 of this thesis describes the experimental setup that was built and explains the design choices that were made. In addition to the detailed description of the setup, the choice to work with ^{87}Rb is explained as well as the basics of Rydberg physics that had an influence on the design of the setup.

Next, chapter 3 of this thesis covers the construction of the vacuum system, including the homemade vacuum cell, the electric field control setup and the Rydberg atom detection in the room temperature test setup. A detailed description of the construction of the homemade ultra-high vacuum cell is given, including the developed glueing technique. A low polarisation extinction ratio (PER) is important on these cell windows, because in the homemade cell optical experiments will be performed. For example, there the rubidium atoms will be excited to the Rydberg state with a well-defined polarisation. This PER is investigated as well as the vacuum inside the cell. In this cell, the atoms are excited into the Rydberg state and ionised after interaction with the oscillator in order to be able to detect the respective Rydberg state. For the Rydberg detection setup, the working principle is explained and the build setup and its alignment are presented in subchapter 3.2. However, due to time constraints, the setup could not be tested during the work on this thesis.

Chapter 4 discusses the theory and construction of the magnetic transport and absorption imaging at the science chamber. Finally, a first successful test of transporting ultra-cold atoms to the science chamber is presented.

Chapter 5 explains the additions to the laser setup of the experiment which were made during the thesis. A new laser was frequency stabilised using a beat note lock to a reference laser. In addition, the laser output was split into two fibre-coupled arms. These can be controlled independently of each other via an acousto-optic modulator. This laser was set up for future use of Rydberg excitation.

Finally the results are summarised in chapter 6 and an outlook on the further iteration of the experiment is provided.

CHAPTER 2

Overview of the Experimental Setup

In this master thesis, the focus is set on the assembly and construction of the experimental system for a hybrid optics experiment. The entire experimental setup is divided into two optical tables. These two tables are the so-called laser table, on which all required lasers are set up, and the experiment table, on which the main experiment system is built. On the laser table, the necessary lasers for cooling and trapping ^{87}Rb atoms are prepared: The lasers are frequency stabilised and in some cases, intensity stabilised, and coupled into optical fibres which are guided to the experiment table. The laser table will be explained in more detail in chapter 5 where the setup of a laser for imaging and probing is discussed.
In this chapter the experimental setup is described in more detail.

As already mentioned, the experimental setup will include an electro-mechanical oscillator that must be precooled to a few K. Therefore, the experiment will be carried out in a cryogenic environment and in an ultra-high vacuum. This imposes some restrictions on the setup. Different laser beams are used for the preparation of the cold atoms. These beams could cause some heating of the environment due to scattering of photons which would act against the cryogenic environment. Therefore, it is not a feasible option to load the atoms from a background gas in the science region.
For this reason, a two-chamber setup is built, see figure 2.1. The first chamber is the so-called MOT chamber. In this chamber, the cold atoms are prepared. In the second chamber, the so-called science chamber (SC), the experiment will be carried out. This section is planned to be connected to a cryostat in summer 2024. These two main sections work under different pressures. In the MOT section, the pressure is approximately 10^{-10} mbar at the ion pump, and in the section of the SC the pressure is expected to be around 10^{-12} mbar, when the SC is connected to the cryostat due to the effect of cryocooling [22]. One of the main topics of this thesis was to build an appropriate science cell. In this homemade cell, a pressure of 10^{-10} mbar can be reached at the ion pump. This cell is discussed in more detail in chapter 3. The two chambers are connected with a differential pumping tube which allows the transport of atoms from the MOT but maintains the desired pressure difference.

In section 2.1 of this chapter, the cold atom preparation and the MOT chamber are explained. Section 2.2 discusses the science region around the science chamber.

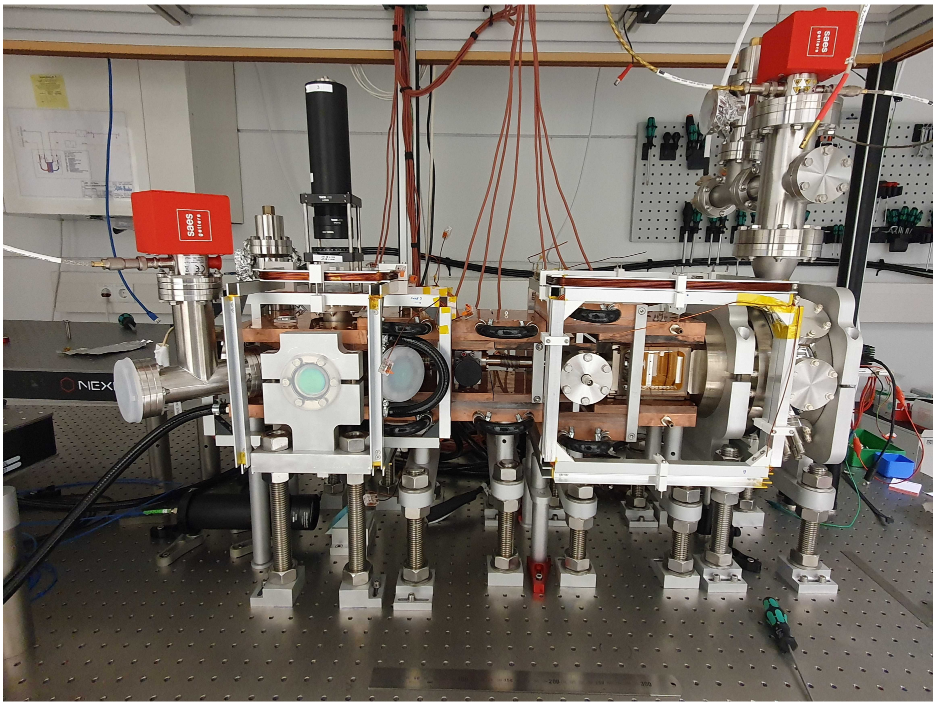

Figure 2.1: The entire physical experimental setup is shown. The setup is divided into two main chambers, which positions are indicated by the two aluminium bias coil cages. The left chamber is the MOT chamber at which the atoms are cooled and trapped with a magneto optical trap. The science chamber, where the experiment will be carried out, is displayed on the right. The science chamber is built on a CF160 flange. To this flange, in the further iteration, the cryostat will be connected. The atoms are moved from the MOT chamber to the science chamber with a magnetic transport. In the copper mounts there are the magnetic coils for the magnetic transport.

2.1 Cold Atom Preparation at Room Temperature

In this section of the experiment, the atoms are prepared at room temperature. The exact parts to build this setup are mentioned in the following as well as how it is built up. Afterwards, it is explained in detail, which atom sources are used and how the design works. The last part gives some technical details regarding the atoms loading.

2.1.1 Vacuum Chamber for Atom Loading

In this section, the exact components for building a setup for cold atom preparation are described. Figure 2.2 shows the MOT chamber of the experiment. In the MOT chamber, ^{87}Rb is cooled and trapped in a magneto-optical trap. The trapping and cooling are done in three dimensions, by using two vertical beams and four horizontal beams and two coils, one above and one below the MOT chamber. In figure 2.3 the fibre outcouplers for the MOT beams are visible. The coils are placed in Anti-Helmholtz configuration. The coils are located in water-cooled copper plates, indicated in figure 2.2 as copper cuboids. The beams are coming through round viewports on the MOT chamber. On the MOT chamber, nine CF40 Kodial viewports [23] are mounted, six for the MOT beams and two for absorption imaging at the MOT chamber. These eight windows have a single-wavelength

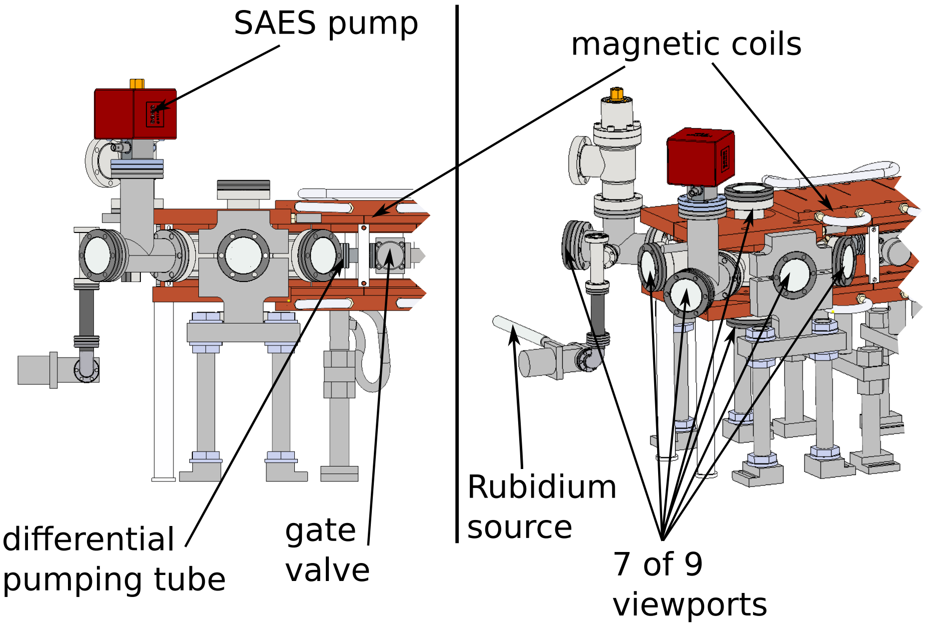

Figure 2.2: Overview of the cold atom preparation setup at room temperature. The setup is shown from different angles and different components are labelled.

AR-coating at 780 nm at a 0° angle of incidence on both sides. The ninth uncoated viewport is mounted along the y-axis and is used for detecting the fluorescence of the MOT. Opposite of this viewport is a CF16 flange on which the custom-designed differential pumping tube from Kurt J. Lesker is attached. The differential pumping tube is a tube with an inner diameter of 4 mm and length of 105.3 mm which results in a conduction of around 10^{-4} L/s [24]. At an expected pressure of 10^{-10} mbar in the MOT chamber and 10^{-12} mbar in the SC the mean free path for rubidium is 4.2×10^{7} m and 4.2×10^{9} m, respectively, at 300 K. Therefore, only a small amount of particles move from one chamber to the other so that the two chambers can be connected, but the pressure in each chamber can be maintained. A CF16 gate valve[1] is mounted behind the differential pumping tube. With this gate valve, it is possible to disconnect the two chambers from each other. This is important, whenever one of the two chambers is opened. For example, the vacuum in the SC has to be opened every time when the sample on the chip is exchanged. At this point, the gate valve can be closed and the pressure and the atomic background gas in the MOT chamber are preserved.

Bias coils are mounted around the MOT chamber to annul the unwanted magnetic field from outside for example the earth's magnetic field and to define the quantization axis. A combined NEG and ion pump[2] is connected to the MOT chamber. The atoms in this experiment are rubidium atoms. The atom source is 5 g rubidium in an ampule[3]. A CF16 gate valve[4] can separate the rubidium source from the MOT chamber when the vacuum has to be opened at the MOT chamber.

---

[1] CF16 Gate valve: 515-GV-C16 from allectra

[2] NEXTorr®Z 200 from SAES[25]

[3] Rubidium 99.75% from Thermo Fisher Scientific Chemicals[26]

[4] CF16 manual UHV gate valve from Pfeiffer Vacuum [27]

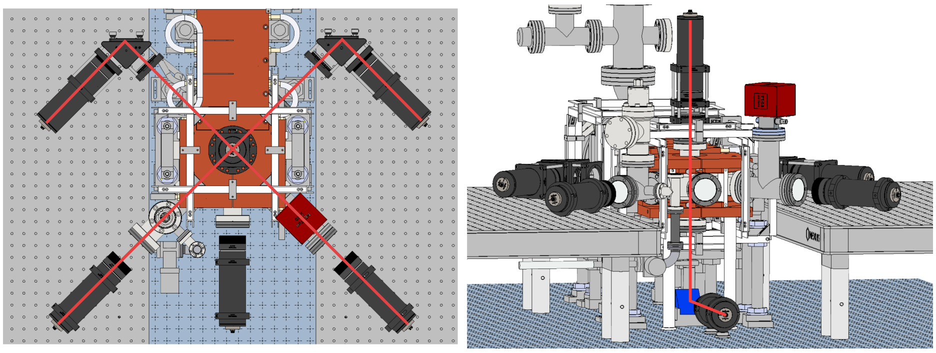

Figure 2.3: The left image shows the horizontal MOT beams looking at the MOT chamber from above. In the right image, the MOT chamber is viewed from the front, and two vertical MOT beams are indicated. With this construction the atoms can be trapped in three dimensions.

With this setup, the cold atoms can be prepared. The rubidium source will be discussed in the following.

2.1.2 ^{87}Rb Atom Source

This experiment works with ^{87}Rb atoms. This subsection will introduce ^{87}Rb as a choice for the cold atom experiment. Also, the construction of a source which evaporates rubidium in a controlled way as a background gas to the preparation chamber is discussed in more detail.

Rubidium

The general choice of rubidium has technical and historical reasons. Firstly, the cold atom preparation is well known and understood [28]. Additionally in this experiment, the atoms will be excited to a highly excited state, the Rydberg state. Alkali metals are a good choice for this type of excitation, as alkali metals only have one valence electron in the outer shell. Therefore, the level structures are simple. This makes the alkali metals very suitable for Rydberg excitation. In addition to rubidium, other alkali metals can be used for Rydberg excitation, for example, caesium [29]. Nevertheless, it is possible to excite other elements besides alkali metals to the Rydberg state [30], like in the sister experiment of this experiment, the YQO experiment (ytterbium quantum optical experiment).
Rubidium has naturally occurring two isotopes, ^{85}Rb and ^{87}Rb[31]. Although natural rubidium consists of 72.17(2)% ^{85}Rb[32] and only of 27.83(2)% ^{87}Rb [33], ^{87}Rb is used in this experiment. This choice is based on two properties of rubidium. One is, that ^{87}Rb has a less complicated hyperfine structure[33]. The other reason is, that the scattering length is positive [34], which results in better evaporation cooling, where the interaction between the atoms is repulsive. This means it is possible to achieve a high density with low temperature with ^{87}Rb which in principle would make it possible to create a Bose-Einstein-Condensate (BEC) [34, 35]. This property could be relevant for the atomic density above the planned atomchip.
In figure 2.4 the level structure of ^{87}Rb is shown. In the level structure, the laser transitions of the Cooler laser and the Repumper laser are shown. The names of the lasers are chosen such that their names describe their mechanism in the procedure of the magneto optical trap (MOT) where the atoms are cooled and trapped. These two lasers are required in the cooling process of the atoms to achieve a

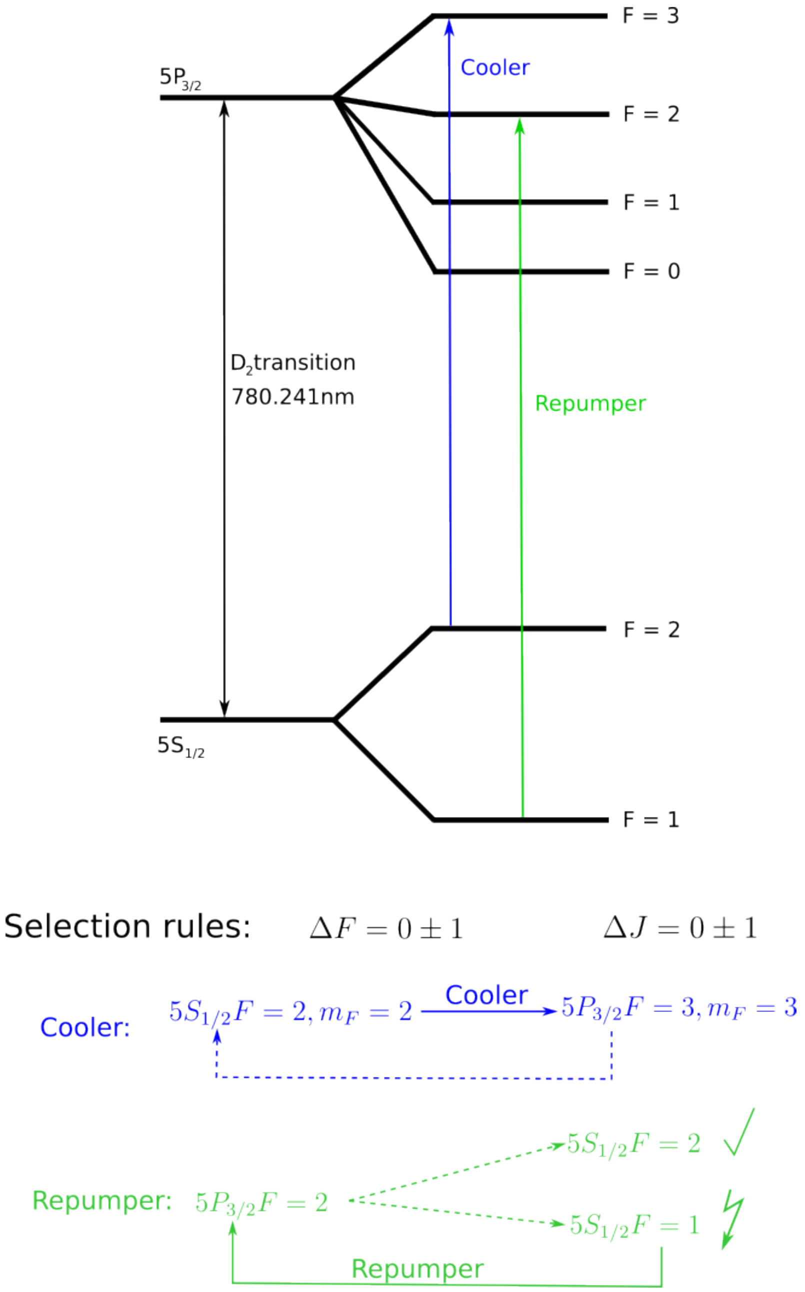

Figure 2.4: The ^{87}Rb level structure and the schematic principle of the laser cooling. In the level structure, the Cooler and Repumper transition is drawn. Below the schematic principle of Cooler and Repumper transition is shown. The dashed line indicates spontaneous emission.

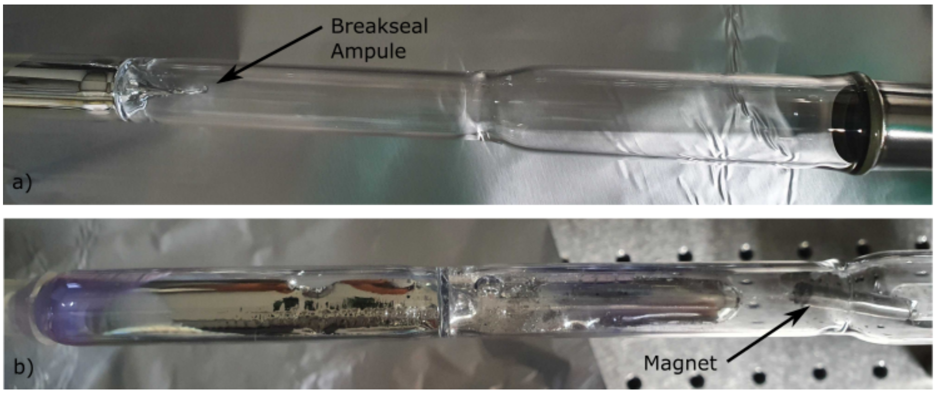

Figure 2.5: The rubidium ampule attached on the glass-metal-transition. In a) the ampule seal is not broken. In b) the breakseal of the ampule is smashed with the magnet. The rubidium was also heated to see if the opening of the smashed break seal was large enough that the rubidium could enter it.

temperature in the μK-regime. The cooler laser excites the atom from the ground state $|5S_{1/2}F = 2\rangle$ to $|5P_{3/2}F = 3\rangle$. Because of the selection rules ($\Delta F = 0, \pm 1$ and $\Delta J = 0, \pm 1$), the state can only deexcite via spontaneous emission to the ground state $|5S_{1/2}F = 2, m_F = 2\rangle$. To obtain this cooling cycle the Cooler laser has to be σ^+ polarized. But the polarisation is not perfect and the Cooler laser has a certain line width, therefore the transition from the ground state $|5S_{1/2}F = 2\rangle$ to $|5P_{3/2}F = 2\rangle$ is possible. The state $|5P_{3/2}F = 2\rangle$ can deexcite to the ground state $|5S_{1/2}F = 2\rangle$ but also in the state $|5S_{1/2}F = 1\rangle$. For the later state, the atoms would be out of the cooling cycle and would no longer be cooled. To bring these atoms back to the cooling cycle the Repumper laser is used. The Repumper pumps the atoms from the state $|5S_{1/2}F = 1\rangle$ to $|5P_{3/2}F = 2\rangle$. This state can again deexcite in $|5S_{1/2}F = 2\rangle$ or $|5S_{1/2}F = 1\rangle$. This pumping is repeated until the atom is again in the $F = 2$ state, where it can be cooled again. This procedure is also schematically shown in figure 2.4.

Design

The rubidium atoms are provided with a 5 g source in an ampule, as mentioned above. The ampule is shown in figure 2.5 and was attached to a glass-metal transition[5] by a glassblower from the chemical institute in Bonn. A magnet is located in the glass-metal transition, which was used to break open the ampule using an external magnet. In order to transfer the rubidium from the ampule or the glass-metal-transition into the MOT chamber the rubidium is heated. By heating the rubidium the vapor pressure increases [33]. To heat the rubidium, heating wires are wrapped around the rubidium source and the connecting tube from the rubidium source to the MOT chamber. The rubidium ampule is heated to around 26 ° C. The connecting tubes are heated up to a higher temperature of around 33 - 40 °C to prevent deposition of rubidium on the walls of the connecting tubes. The wire-wrapped parts are wrapped in aluminium foil to prevent heat loss to the environment. The construction is illustrated in figure 2.6. This source creates a background gas in the loading chamber for starting the experimental cycle with a MOT.

---

[5] Glass metal transition (Pyrex and 304 stainless steel), open end from Accu-glass products[36]

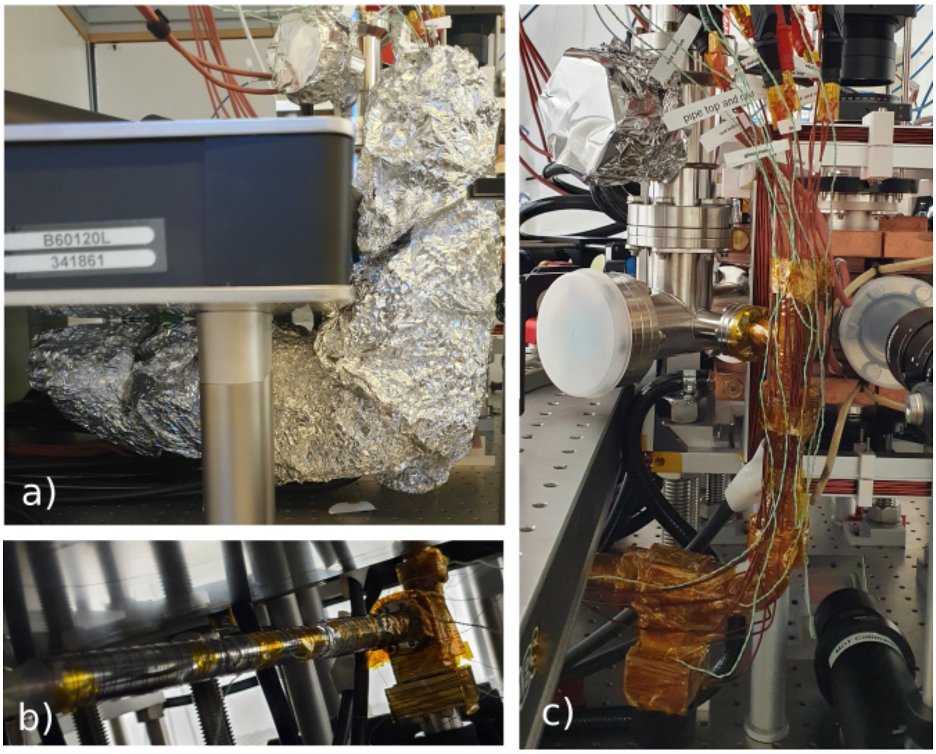

Figure 2.6: Rubidium ampule wiring construction. In a) is the rubidium ampule and the connecting tube wrapped in aluminium foil to isolate the construction better from the environment and get a stable temperature. b) and c) show the construction under the aluminium foil layers. In b) a closer look at the wiring of the rubidium ampule and the gate valve. In c) the wiring of the gate valve and the connecting tubes are shown. The white/green cable is used for temperature measurement and the yellow Kapton tape to avoid a short circuit.

2.1.3 Atom Loading

This section describes the atom loading in more technical detail.
The atoms will be trapped and cooled in this experiment with a magneto-optical trap (MOT) in three dimensions. For this trapping, two coils in an Anti-Helmholtz configuration and three laser pairs with counter-propagating direction are used. The handness of the horizontal beams has an opposite handness as the horizontal beams. The $1/e^2$ diameter of the MOT beams is approximately 37.5 mm. The power of each MOT beam is approximately 70 mW. Two transitions are required for a successful MOT, see section 2.1.2. For this transition, a Cooler laser and a Repumper laser are used. These laser beams are frequency and intensity stabilised. To overlap these two beams two polarisation maintaining fibre beamsplitters are used, one for the horizontal MOT beams and the other one for the vertical MOT beams. The used fibre beamsplitters have two inputs for the Cooler laser and the Repumper laser. The fibre beamsplitter for the horizontal MOT beams has four outputs and the fibre beamsplitter for the vertical MOT beams has two outputs. The polarisation of the beams is set with an $\lambda/4$ waveplate in front of the MOT chamber.

2.2 Cryogenic Chamber for Rydberg Experiments

In this section, the second main part of the experimental setup is explained. This experimental setup section contains the science chamber where the experiment will be carried out and the Rydberg atom detection. The assembly of these two parts are explained in more detail in chapter 3. In this section a short overview of the Rydberg physics is given in 2.2.1 and the setup of the science region is described in 2.2.2.

2.2.1 Considerations for Rydberg Hybrid Setups

In this section, Rydberg physics is briefly explained so that some of the decisions and efforts involved in the design and construction of this experiment can be better understood.

Rydberg atoms are atoms with at least one electron highly excited to a principal quantum number n, typically $n > 10$ [37]. In this experiment, it is planned to work with a Rydberg state of $n = 68$ or $n = 85$. At this high excitement the exited electron, the Rydberg electron, has a small overlap with the nucleus and the inner electrons, which results in some notable properties [16]. One of the properties is that the binding energy of the Rydberg atoms is low, which leads to a high sensitivity to electric and magnetic fields. Due to this sensitivity, the lifetime of the Rydberg atoms, in addition to spontaneous decay to lower energy levels, depends on the background light in the system. The lifetime of $n \gtrsim 40$ is dominated by the absorption and stimulated emission of infrared modes generated by non-zero temperature objects in the environment [16]. To avoid this dominance, a cryogenic environment around the Rydberg atoms can be used [16].

The atom can be excited with different methods to the Rydberg state [38, 39]. In this experiment, the atom is excited with optical excitation. For one photon excitation, the wavelength would be in the UV regime and the desired S-state can not be reached, because of selection rules [16, 40]. So in this experiment, a two-photon excitation will be used. Hereby the excitation goes from the ground state $|g\rangle = |5S_{1/2}\rangle$ to the Rydberg state $|r\rangle = |nS_{1/2}\rangle$, using the intermediate state $|i\rangle = |5P_{3/2}\rangle$. The transition from $|g\rangle$ to $|i\rangle$ is driven with a weak probe field and the transition from $|i\rangle$ to $|r\rangle$ is reached with a strong control field. The setup to drive this transition is called probe-control-setup. Both fields can be tuned in power and frequency. The detuning of the probe field with respect to the intermediate state results in avoiding some spontaneous scattering on the intermediate $5P$-state [16]. The control field can then be tuned to compensate the probe field detuning and into resonance with the Rydberg state. This leads to an effective two-level schema. This procedure is also called adiabatic elimination [41].

2.2.2 Vacuum Chamber Design for Hybrid Experiments

The experiment is carried out in the second main section of this experiment. The science region is shown in 2.7.

The experiment will be carried out in the homemade glass titanium vacuum cell. The construction of this cell is explained in more detail in chapter 3.1. In this master thesis, the SC is connected to an octagon[6]. The octagon has eight CF40 flange connections, one is used for the pump section. In the

---

[6] Spherical octagon vacuum chamber from Kimball Physics [42]

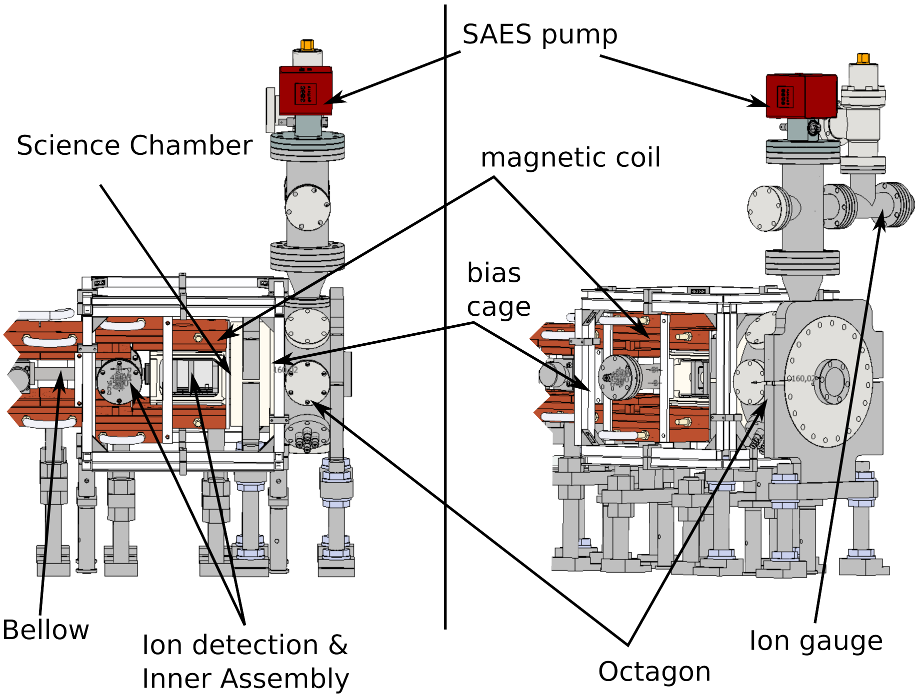

Figure 2.7: CAD sketch of the science region with a pump section at room temperature. Different parts of the science region setup are labelled.

pump section a combined NEG and ion pump[7] is connected and an ion gauge[8] to monitor the pressure. The octagon and the pump section will be replaced by the cryostat in the next iteration. Besides the one CF40 connection on the octagon to the pump section, two other CF40 connections are used, the remaining CF40 connections are closed with CF40 blind flanges. On the two CF40 flanges, SHV (safe high voltage) CF40 feedthroughs[9] are mounted. These feedthroughs are connected to the inner assembly to supply the electrodes on the inner assembly with power. The inner assembly is placed in the SC and is the first part of the Rydberg atom detection and the ion detection, respectively.

A cross tube[10] is mounted on the SC with a CF16 connection. In the crossed tube a deflection electrode is placed. The cross tube has two CF40 flanges opposite from each other and two CF16 flanges. The deflection electrode inside of the cross tube is the second part of the ion detection and is mounted on a CF40 feedthrough, which in turn is mounted on the cross tube. Opposite of feedthrough a MCP (micro channel plate) is mounted on the cross tube. The MCP is the third and last part of the ion detection and is used to detect the ions. The ion detection is explained in more detail in chapter 3.2.

The second CF16 flange of the cross tube, which is opposite of the SC, is mounted to a CF16 bellow[11]. The bellow is connected to the gate valve, which can disconnect the two chambers. A bellow is used to maintain a certain degree of freedom in relation to the MOT chamber when aligning the SC.

---

[7] NEXTorr® D500-5 from SAES[43]

[8] Ion gauge UHV-24p (dual thoria/iridium filament) from Agilent

[9] SHV CF40 feedthroughs from Allectra[44]

[10] CF40-CF16 reducing cross tube from Kurt J. Lesker, custom design

[11] CF16 bellow from Allectra, custom design, 89 mm ± extension/compression; 316L stainless steel

From the MOT chamber to the SC, magnetic coils are attached in copper cuboids to transport the cooled and trapped atoms to the SC, see also chapter 4.2. Black hoses for the cooling water are attached to the copper cuboid. Temperature sensors and power cables for the coils are also connected. A bias coil cage is mounted around the SC.
The MOT chamber was already placed on the experiment table by starting the thesis. The cryogenic science region was set up in this thesis as well as the magnetic transport. The assembly of the various parts is explained in more detail in the following chapters.

CHAPTER 3

Construction of the Vacuum System

In a further iteration of the experiment, highly excited atoms, so-called Rydberg atoms, are coupled to a microwave source. The lifetime of the rubidium atoms in the magnetic trap is limited by collision with the background gas [22]. Therefore, an ultra-high vacuum chamber is required. In this thesis, the focus was on building this ultra-high vacuum chamber. Section 3.1 describes in detail the procedure of glueing a homemade titanium glass vacuum cell. Additionally, the investigation of the vacuum cell after the glueing process is described. Inside the vacuum cell, an assembly of electrodes is mounted. This inner assembly will be used for ionisation of the Rydberg atoms. The Rydberg ions can be detected after ionisation. This ion detection can be used to determine which Rydberg state the atom was in and whether there was an interaction between these two physical systems. Section 3.2 deals with the Rydberg detection. Firstly, the theory is explained and then the design and assembly of the ion detection is described.

3.1 Home Build Titanium-Glass Vacuum Cell

As described in chapter 2, the experimental setup consists of two sections: A MOT chamber, which has already been discussed, and a science chamber, which was fabricated as part of this thesis. This chapter focuses on the homemade science chamber (SC). First, the motivation to build a vacuum cell homemade, instead of buying one is given in section 3.1.1. Furthermore, the reason behind the chosen design and the procedure of glueing a vacuum cell is presented in the following sections 3.1.2, 3.1.3 and 3.1.4. Section 3.1.5 reports on the performance of the glued cell, in particular with regard to the pressure achieved before and after the bake-out.

3.1.1 Motivation

For the planned experiments where an atom chip is combined with a cloud of ultra-cold atoms, a vacuum cell for ultra-high vacuum (UHV) with some degree of optical access is required. Further, the vacuum chamber must have two connecting flanges, such that it can be attached to both the MOT chamber and to the planned cryostat.
One possibility could be to use a vacuum cell which is constructed only of glass beside the flanges, for example from Infleqtion [45]. Such a glass cell offers a large optical access but is only sold in certain sizes and usually with only one connection. As mentioned above, this setup requires access from two

sides. It is possible to buy customised glass cells with two flanges, but an additional port can exert large stresses on the glass cell that can cause the glass to break.
Another possibility is to assemble a vacuum chamber from commercial parts as is done for the MOT chamber: An appropriate chamber is chosen, such as an octagon, for example from Vacom. For optical access round view ports are screwed on the cell, which results in lower optical access compared to the cells, which are only constructed of glass. Additionally, these cells have a certain height due to the view ports. In this experiment, a small height is required since the atoms will be transported and trapped in a magnetic trap. It is therefore crucial that the coils can be mounted tightly around the vacuum chamber since the magnetic field scales with r^{-3}[46].
With a certain work volume and the necessity to get the magnetic coils as close as possible to the work volume, a commercial solution is not optimal. Therefore, the choice fell on a homemade glass cell. The glass vacuum cell consists of a titanium frame. The cell constructed in this thesis is the second generation of homemade vacuum cells in the research group.

3.1.2 Design

This section describes the design of the homemade glass vacuum cell. In order to motivate some design changes from the first-generation vacuum cell to the second-generation vacuum cell, the problems of the first-generation vacuum cell and their possible causes are first explained. Then the general design is described with an overview of the materials used, followed by the small design changes.

The first generation glass titanium cell was assembled in spring 2023, pumped under vacuum, and baked to 130 °C for one week. However, defects were noticed on the windows after the bake-out, see figure 3.1, although it is unclear whether the defects occurred during the glueing process or later during the bake-out. Although the defects were not located in the area relevant for optical access, it was not clear why they appeared. One possibility could be that the defects are caused by baking out in a non-clean area, meaning in a dusty environment. However, the glass cell has to be connected to the MOT chamber, and the entire assembly has to be baked out altogether. This means that there is a possibility that more defects could be created in the relevant areas during the final bake-out. As a result, it would be a possibility that the cell has to be replaced because the experiment could no longer be carried out sufficiently well with defects in the optically relevant area.
The first-generation glass cell also had another important problem: It developed leaks. The first pump-down before baking showed vacuum pressures of 1.6×10^{-8} mbar. In addition, a helium leak check was done. During a helium leak check, helium is flowing from outside around the experimental setup and with a residual gas analyzer (RGA) the helium amount in the system is measured. When helium can enter through a leak, the measured helium value goes up, showing that the setup has a leak at the tested position. Before the bake-out, no leak was found. After the bake-out, however, a helium leak check showed that the glass cell was not tight. It is assumed that the leak developed during baking. This effect is explained in section 3.1.5. However, the leaks were successfully sealed with a high vacuum leak sealant Vacseal®from Allectra [47]. Therefore the first-generation vacuum cell was connected to the experimental setup. After connecting all different parts of the experimental setup, a helium leak check was done for the experimental setup. Unfortunately, some leaks were found at different positions in the setup. Due to the bad performance of the first-generation of the cell, it was decided to build a second-generation of the cell. The cell design was therefore slightly changed, and the glueing technique was improved.

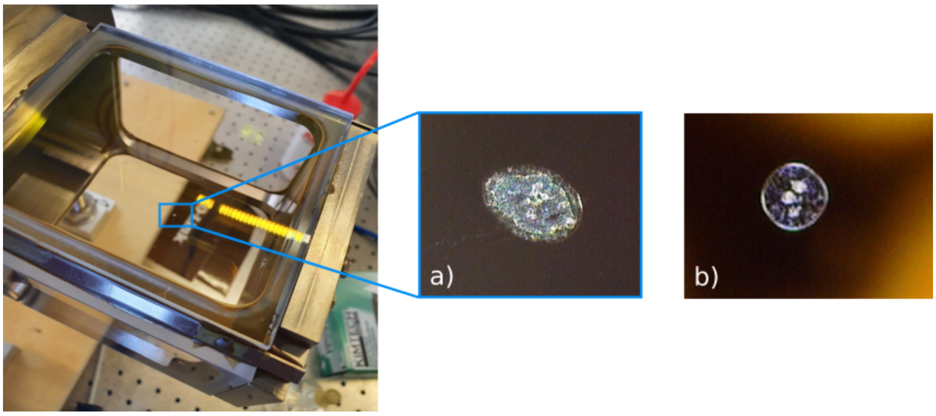

Figure 3.1: Examples of defects on the first generation vacuum chamber windows. Microscope images of different defects on different positions are shown in a) and b).

object	Dimension [mm]
titanium frame (outer)	124 × 86 × 106
inner experiment region	30 × 30 × 30
inner heat shield	121.5 × 53 × 33
outer heat shield	121.5 × 66 × 46
small window	100 × 70 × 6
wide window	100 × 90 × 6

Table 3.1: Dimension of the different objects from the science chamber

To summarise, the two problems of the first-generation vacuum cell were the defects on the window and the leaks.

In the following, the design of the vacuum cell in general is described first and then design details that have changed from the first vacuum cell to the second vacuum cell.
As already mentioned, the glass cell consists of a frame made out of titanium, see figure 3.2. Glass windows of N-BK7 are glued to the frame with two-component vacuum-compatible epoxy glue [48]. The frame is made out of titanium because it is necessary to have the same thermal expansion coefficient of the windows and the frame to avoid unnecessary stress on the windows during bake-out. Shear on the glue can cause some cracks in the glue itself, which can lead to leaks. That is why these specific materials have been chosen, as they have nearly the same thermal expansion coefficient χ_{thermal}. Titanium has a thermal expansion of $\chi_{\text{thermal,Ti}} = 8.6 \times 10^{-6}/\text{K}$ [49] and N-BK7 glass of $\chi_{\text{thermal,N-BK7}} = 8.3 \times 10^{-6}/\text{K}$ [50].
The outer dimensions of the titanium frame are shown in table 3.1. These dimensions were chosen because it was decided to have a volume of 30 × 30 × 30 mm to carry out the experiment. Around this volume and inside the chamber heat shields are installed. The heat shields are used to cool down the environment of the trapped atoms and shield the atoms from background radiation. These heat shields have a certain dimension mentioned in table 3.1. The outer shielding specifies the minimum size of the inner volume of the titanium frame. As the vacuum chamber should have

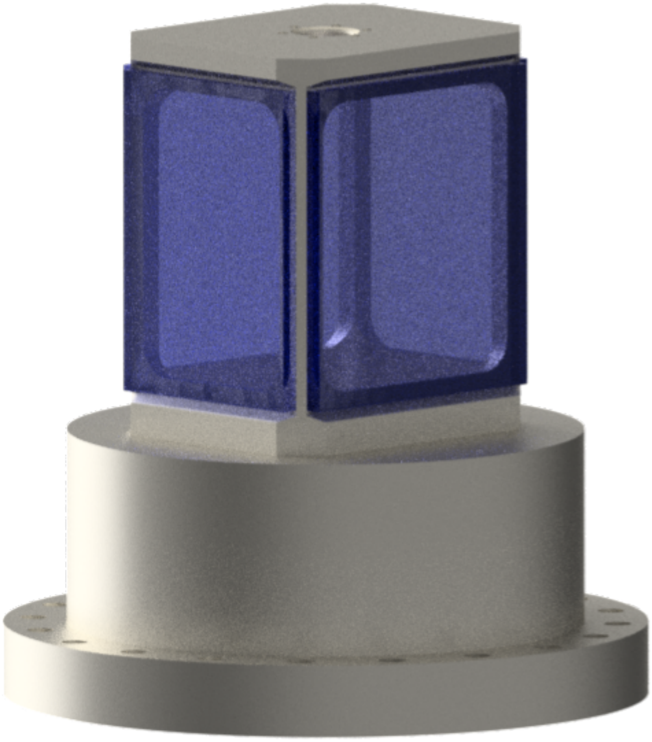

Figure 3.2: Design of the homemade science chamber. The frame is made of titanium and the windows are made of N-BK7 glass. These two materials are glued with a two-component epoxy glue.

the smallest possible outer dimensions due to the magnetic trapping field, the vacuum chamber has this selected outer dimension, see table 3.1. The vacuum cell has a high optical access with large window dimensions as given in table 3.1. The titanium frame was made by the mechanical workshop of this institute. The windows from Lens-Optics are made of N-BK7 material and have a AR/AR 420 - 480 nm and 780 - 1 064 nm coating. These anti-reflection coatings are chosen for the wavelengths needed to do two-photon excitation of rubidium to Rydberg states, see chapter 2.2.1.

Since glue bonding failures during bake-out were the main problem of the first cell, the design of the second cell was slightly changed, see figure 3.3. In the corners are round cutoffs of 4 mm diameter to prevent running out of the glue. The frame is cut out in such a way that the grooves are 27° angled, and a space of 0.5 mm is left between the titanium frame and window when the window is placed in the centre. With this design, the opportunity is given to get an additional glue sealing layer on the side of the window and simplify the placing of the windows in the frame centre.

3.1.3 Preparation of Gluing Process of the Titanium Cell

It is crucial to work in a clean environment and with clean tools when glueing and curing the vacuum cell. This is because dust and other particles can cause some defects on the windows or cause less

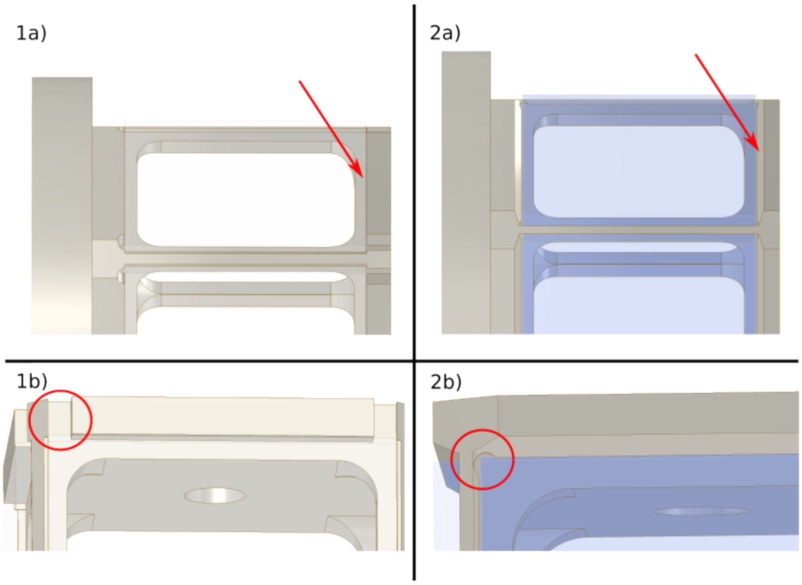

Figure 3.3: Design details of the first-generation and second-generation vacuum cell. The number 1 indicates the first-generation design and the number 2 indicates the second-generation design. In a), the first-generation has titanium frame edges with 90° and the second-generation with 27°. Thereby the glue can also bond from the side of the window. In b) the different designs of the corners are shown. In 1b) a cut in the titanium frame was done in such a way that the glue could flow outside. In 2b) the design was changed to a closed circle to prevent running out of the glue.

adhesion between the windows, the glue and the titanium frame. For this reason, the titanium frame was cleaned with two different methods. First, the titanium frame was cleaned with chemical solvents to remove dust or organic smears from the surface. For this procedure, only chemical solvents with a high purity are used to avoid some dirt caused by the solvents on the UHV parts. Secondly, the titanium frame was treated by atmospheric plasma to remove organic contaminates shortly before applying the glue. Both methods are explained in more detail in the following.

UHV Cleaning

The titanium frame was cleaned by rinsing it in an ultrasonic bath in four different detergents. The titanium frame is a relatively large part. Therefore, a metallic bin was used with dimensions of 28 × 23 × 19 mm. This bin was cleaned with normal water and soap and afterwards rinsed with normal water to remove dust and smears from the bin. A small amount of Sonoswiss Cleaner T1 (SW-C T1) from Sonoswiss, which is diluted 3-5% by volume with demineralised water was poured into the bin until the volume was enough to cover the titanium frame. The titanium frame was put in the bin in such a way that the knife edge of the titanium frame had no contact with the bin to avoid damage to the knife edge. The bin was then put in a large ultrasonic bath for one hour at 70 °C. After one hour titanium frame was rinsed with demineralised water. The bin was rinsed too, while the titanium frame was laying on an isopropanol-cleaned aluminium foil layer. Afterwards, the titanium frame was sonicated in the bin in demineralised water for 10 min to remove any soap leftovers After this step, the demineralised water was removed and the bin was rinsed with acetone, while the titanium frame rested again on a newly cleaned aluminium foil layer. The titanium frame was dried with pressurised air and then sonicated for one hour in acetone. A second clean with isopropanol bin was prepared during the sonication. The second bin is prepared since the next step has to go fast. Acetone evaporates relatively quickly [51] and the evaporation could leave dissolved residues on the titanium frame. To avoid dirt the titanium frame was rinsed with isopropanol after finishing the acetone ultrasonic bath and placed afterwards in the prepared second bin with isopropanol. The titanium frame was sonicated in isopropanol for 15 min. After finishing the sonication, the titanium frame is placed on a cleaned aluminium foil and dried with pressurised air. When the titanium frame was dry, it was wrapped with cleaned aluminium foil while care was taken to not damage the knife edge. The titanium frame was wrapped in aluminium foil for safe storage and to maintain the vacuum cleanness of the titanium until windows are glued onto the frame.

Cold Atmospheric Plasma

When two surfaces are glued together, the surfaces must have a high wettability, because the wettability is an indicator of the extent to which the solid surface is attractive to the liquid, which means how strong the adhesion between the solid surface and the liquid is. This property of high wettability is not always given even if the material surface is cleaned. A low wettability decreases the adhesion of glue to the material [52]. A low wettability can be caused by a low surface energy. The surface energy describes the excess energy on the surface compared to the bulk energy of the material. In a solid material, the atoms in a bulk are normally stable and have an organized bonding and interaction, respectively. On the surface, the interactions are not balanced and so the surface atoms have unrealised bonding energy, which results in the surface energy [52]. The surface energy is correlated to the bulk energy. Therefore metals have naturally a high surface energy. In liquids, the same phenomena are found but are described with surface tension. The surface tension describes the cost to increase the area of the liquid [53].

The material always wants to decrease its surface energy. This can be achieved by absorbing a material with a lower energy onto its surface. Due to the weaker inner bonding of the liquid, the surface tension of the liquid is often smaller than the surface energy of the solid. Therefore the applied liquid on the solid surface will be spread to a specific degree over the solid. This wettability can be measured with the contact angle θ_C [54]. The contact angle θ_C describes the angle between the liquid and the solid surface. By increasing the surface energy or reducing the surface tension, the wettability is increased. The increased wettability can be measured with a reduced contact angle, see figure 3.4. This behaviour is also described with the Young's equation [54]

$$\gamma_S = \gamma_{SL} + \gamma_L \cos\theta_C,$$

where γ_S is the solid surface energy, γ_{SL} the interfacial surface tension between surface and liquid and γ_L the liquid surface tension. In this case, the glue is the liquid and the NBK-7 window glass and the titanium frame are the solids. To obtain the best wetting, these two solid materials are not only cleaned with organic solvents but also treated with atmospheric plasma treatment (APT).

APT can be used for fine-cleaning of surfaces and to increase the surface energy of a material. These two effects are described in the following in detail regarding the two materials on which the cold atmospheric plasma is used in this thesis, the titanium and the N-BK7 glass.

With the treatment of cold atmospheric plasma on the glass the surface energy is increased by

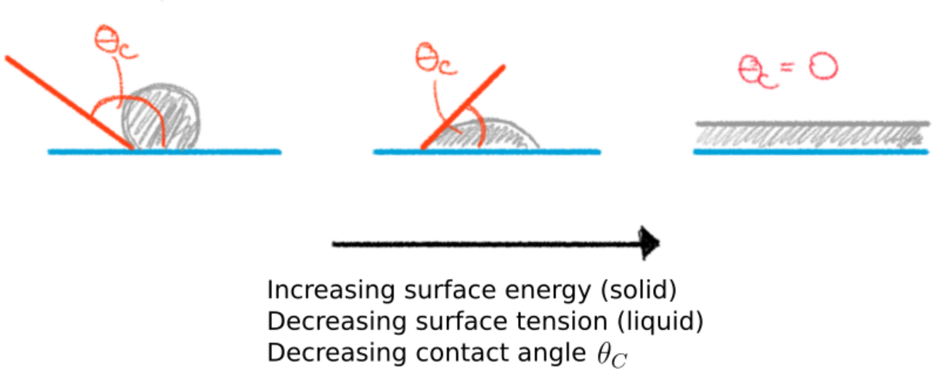

Figure 3.4: A sketch of the contact angle of a liquid droplet on a solid surface, depending on the surface energy and surface tension. Increasing the surface energy or decreasing the surface tension increases the wettability. The wettability can be measured with the contact angle θ_C.

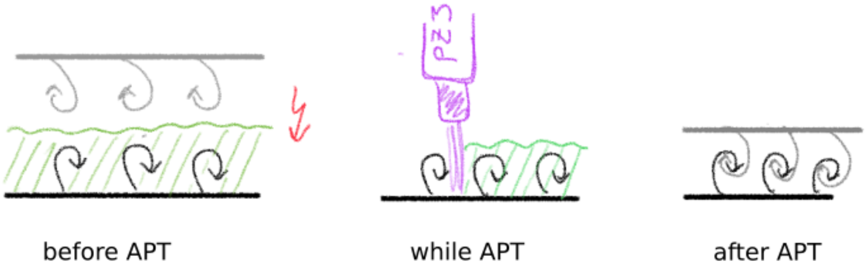

Figure 3.5: A sketch of the binding sites of the glue and titanium before, while and after APT. Before APT the anchor groups are covered with organic contamination and the anchor groups of glue and titanium can not react with each other. The APT removes the organic contamination. After APT the anchor groups of titanium are reachable for the anchor groups of the glue.

integration of polar groups [52]. Therefore the bonding of the glue and the glass can get stronger [52] [55].

Metals have, as mentioned above, naturally high surface energy. Nevertheless, the atmospheric plasma treatment is used on the titanium frame. This is done because the binding sites of the titanium could be covered by a couple of monolayers of contaminants, indicated in figure 3.5 as anchors. The atmospheric plasma removed the contamination layers by ablation and the binding sites are available [52]. Thereby the adhesion of glue and titanium can be increased.

3.1.4 Gluing Process of the Titanium Cell

In this section, the glueing process of the second titanium cell is explained step by step.

The glue process was done in an ISO class 5 cleanroom under a fume hood, except for curing the cell and degassing the glue. This was done in an ISO class 6 cleanroom. The classes refer to the number of particles of a certain size. In an ISO class 5 cleanroom there are $10^5/\mathrm{m}^3$ and ISO class 6 cleanroom there are $10^6/\mathrm{m}^3$ of $\geq 0.1\,\mu\mathrm{m}$ particles, respectively [56]. The glueing of the vacuum cell was done in the cleanrooms for pollution reduction, for example, dust particles, on the surfaces of the titanium frame and windows, respectively, which could cause less adhesion of the glue and cause the generating of leaks. Small particles could also be the reason for the defects on the windows as explained in section 3.1.2

In the following the glueing procedure is described in detail. This procedure was done for each of the four windows.

The first step was the *mixing of the two components of the glue* to get a homogeneous mixture. The used glue is the epoxy H77S glue[1], which is a two-component glue with a mix ratio by weight of 100:35. This glue is used, because it has a small particle size ($\leq 20\,\mu\mathrm{m}$) and low outgassing rate [48]. Due to the low outgassing rate, the vacuum is not limited by the outgassing rate of the glue. When mixing the two components it is unavoidable that some air gets trapped in the glue. These air bubbles can decrease the adhesion of the glue on the window. Also, the trapped air bubbles can be problematic during bakeout, as they expand and cause additional stress, which can lead to leaks. In addition, depending on their position, the trapped air bubbles can cause virtual leaks in the vacuum chamber. If air bubbles have a small access to the inside of the vacuum chamber, the air can slowly outgas into the cell, but still fast enough to limit the vacuum inside the chamber. Therefore the air has to be removed from the glue. This was done with a desiccator connected to a diaphragm vacuum pump[2]. The vacuum causes the air bubbles to expand and rise to the top of the glue, where they then burst, see figure 3.6a). While degassing the glue, it was noticed that the two components were separating slightly. The glue was stirred again and after the stirring, the glue was degassed again.

While the glue was degassed the *windows were cleaned* with ethanol to remove the particles on the window surface due to the packing materials.

In the next step *the glue was slowly poured into a syringe*. A special syringe for applying epoxy glue was used. With this type of syringe[3] [4] the air between glue and plunger will not be pushed in the glue but rather flow around the plunger when the plunger is slowly pushed into the barrel. As a result, it can be avoided that air gets trapped in the glue. By applying one glue line on an aluminium foil sheet and inspecting it by eye, it was checked that no air bubbles were trapped in the glue anymore.

In the next step the titanium frame was prepared. The titanium frame was mounted on a self-made construction to get the frame in as good a horizontal position as possible. This is important for the last step: *curing the glue*. In this step, the glue becomes more fluid and flows over the titanium frame. In order to achieve an even distribution of the glue and therefore a good adhesion between the titanium frame, glue and window, the titanium frame should be horizontal. To get a horizontal position the titanium frame was mounted with four rods on a rectangular plastic plate which has the same height as the 160CF flange of the titanium frame. The construction is shown in figure 3.6.

The area of the *titanium frame on which the window will be attached was then polished*, see figure 3.6b). For the polishing, a diamond polishing sheet[5] with a $6\,\mu\mathrm{m}$ particle size was used. The titanium frame was polished to remove the oxide layer of the titanium. This improves the adhesion of the glue to the

---

[1] EPO-TEK®H77S from Epoxy technology [48]

[2] Varian Vacuubrand MV2 Diaphragm pump, M3H 2, Ultimate .6 Torr, KF16 inlet, 110-120 VAC 949-9451[57]

[3] syringe barrel and plunger from Kummer:Semiconductor technology

[4] Needle:Techcon Dosiernadeln TE721050PK [58]

[5] LF6D from Thorlabs [59]

surface of the titanium frame, as the oxide layer adheres less to the metal [60]. The remains of the polishing were removed by wiping the titanium frame with isopropanol, see figure 3.6c).
Subsequently the area of *titanium frame on which the window will be placed was treated with atmospheric plasma* to remove the organic contaminates on the titanium frame. In the section 3.1.3 the atmospheric plasma treatment was described in more detail. The atmospheric plasma is generated by the piezo brush PZ3 from Reylon Plasma [61]. The piezo brush was slowly moved over the surface and with the same distance of around 1 - 2 cm between the brush and the titanium surface, see figure 3.6d).
The next step was to *apply the glue with the syringe to the titanium frame*, where the window will be placed, see figure 3.6e). A single line of glue was applied along the titanium frame. Care was taken that the amount of glue was always the same and that no air bubbles were created. With a new needle the glue was spread evenly over the titanium frame, see figure 3.6f). Again, care was taken to not get air into the glue.
After the glue was prepared on the titanium frame, the *window was cleaned again* with ethanol. Due to the repeated cleaning, it could be ensured that no dust particles are on the window when the window is placed on the titanium frame.
This was followed by *atmospheric plasma treatment on the edges of the window* using the plasma brush, see figure 3.6g). By using the atmospheric plasma on the window the surface energy is increased and as a result, the adhesion between the window and glue is improved as described in section 3.1.3.
Then *the window was placed on the glue and the titanium frame*. The procedure is to place first the short edge of the window on the glue with a certain inclination angle between the window and titanium frame and then lower the window carefully, reducing the inclination angle smoothly until the window is fully placed onto the frame, see figure 3.6h).
Thereafter the *glue connection was inspected* to check whether air bubbles had become trapped during lowering the window. In the best case, no air bubbles are visible, but probably a few air bubbles will be trapped in the glue. As long as the air bubbles have a diameter of less than 3 mm and they are surrounded by glue they were estimated to not be problematic. In the case where a lot of air bubbles were present, or when the air bubbles were near the vacuum edge of a window such that they could produce virtual leaks, the windows were removed again. The window and the frame were then cleaned again, and the procedure was repeated from the step where the *titanium frame was polished*.
The final step was to *cure the glue* in an oven[6], see figure 3.6i). The oven should be cleaned beforehand from dust with isopropanol. The oven was heated linearly from 20°C to 150°C for 2.10h. For 1.10h the temperature was held constant and then the temperature was ramped down to 20°C for 2.10h. The 20°C was kept until the moment when the titanium cell is removed from the oven. With the controlled temperature ramping the glue could be cured with minimal thermal stress.

3.1.5 Inspection of Glued Vacuum Cell

After curing the glue, the vacuum cell was investigated. First, the optical behaviour of the vacuum cell was investigated. Then the cell was analysed with regard to the vacuum in the cell after bake-out.

In the following the optical investigation is described. On the vacuum cell only three defects were found before bake-out, none of them on an optical relevant position, see figure 3.7.
Following this, the cell was investigated with regard to birefringence on the windows. The birefrin-

---

[6] UF260plus oven from memmert [62]

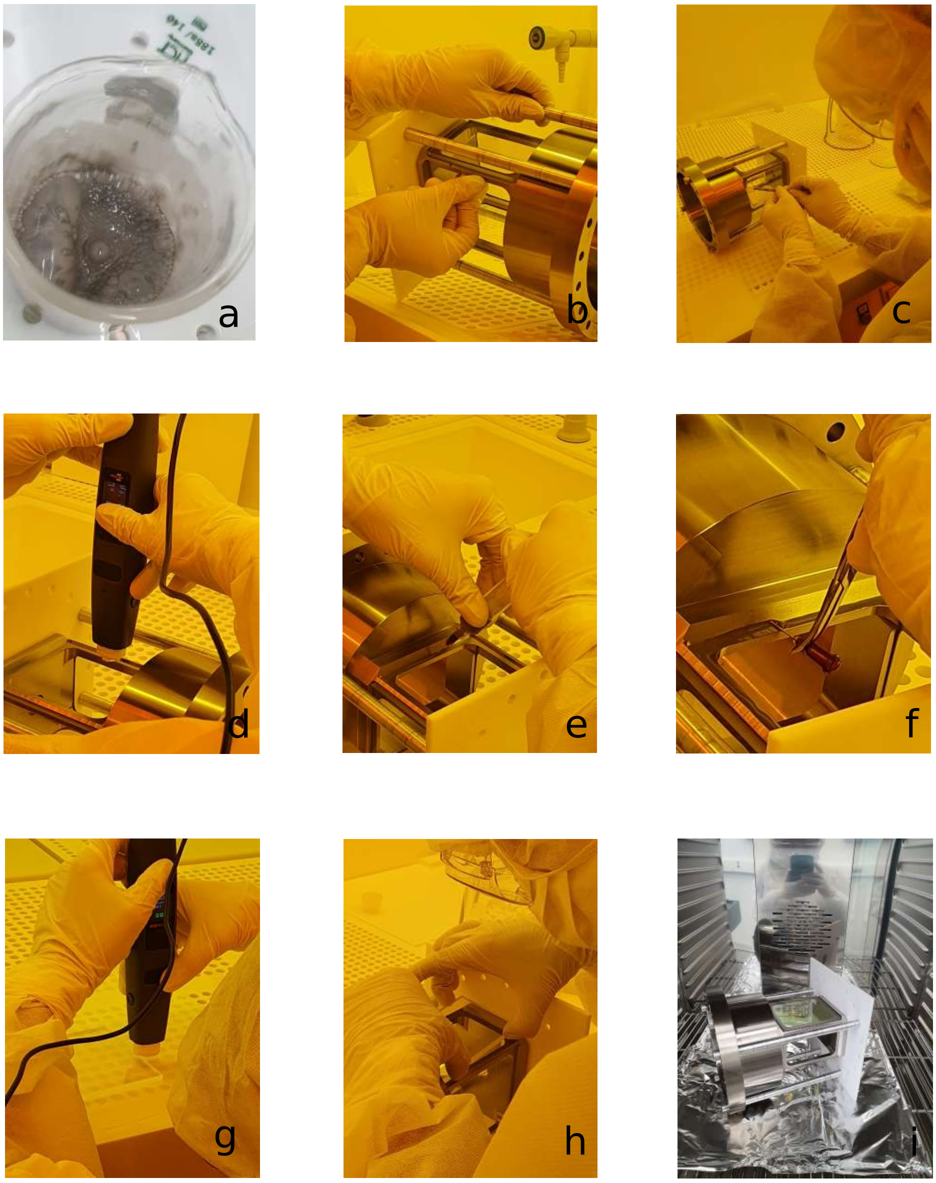

Figure 3.6: Images of different steps of the glueing procedure of the vacuum titanium cell in an ISO class 5 cleanroom. a) Mixed two-component glue (EPO-TEK®H77S from Epoxy technology[48]) is outgassing in a desiccator to remove trapped air in the glue. b) The titanium frame is polished with a diamond polish paper to remove the oxide titanium layer. c) By wiping with isopropanol over the polished titanium frame the remains from the polishing are removed. d) The titanium frame is fine-cleaned with an atmospheric plasma using the piezo brush PZ3. e) With a syringe one line of the glue is evenly applied around the titanium frame. f) The glue is spread over the frame using a needle. g) The surface energy of the glass is increased by the piezo brush PZ3 to increase the adhesion between the glue and the window. h) The window is placed on the glue. The window is first placed with the smaller edge on the glue on the titanium and then the angle of inclination is gradually reduced until the window rests on the glue or the titanium frame. i) The titanium frame with a newly placed window is put in an oven from Memmert. The glue is cured at 150 °C for 1.10h.

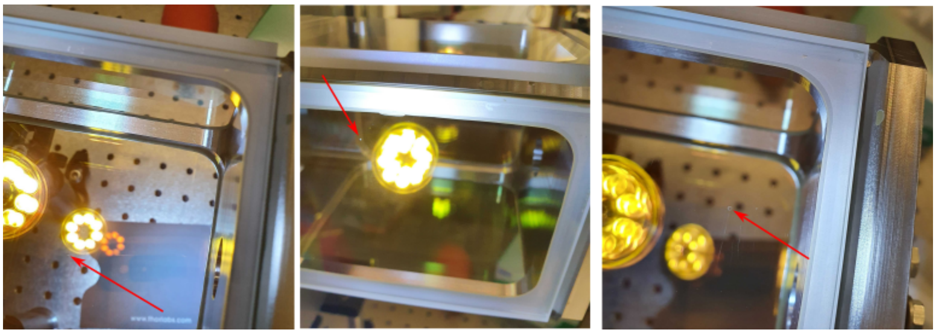

Figure 3.7: Images of the science chamber windows after curing. The three observed defects on the windows are highlighted with a red arrow. The defects are on not optical relevant positions.

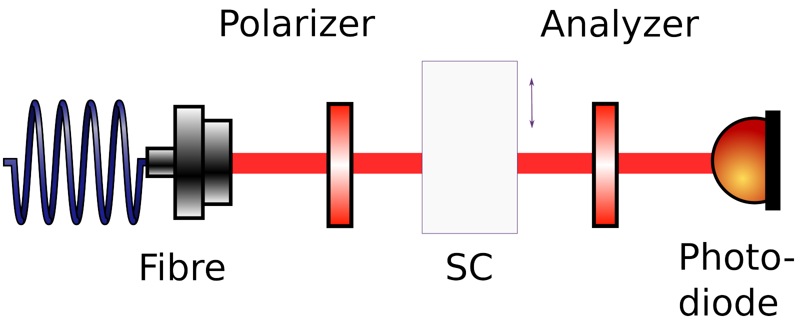

Figure 3.8: The schematic of the setup for the polarisation extinction ratio measurement. The science chamber (SC) was moved perpendicular to the position of the beam so that the PER could be measured at different positions in the SC.

gence can be caused by glueing the windows on the titanium frame, which could apply stress on the windows. Due to birefringence, the polarisation can be changed after passing the vacuum cell, since the s-polarisation and the p-polarisation can be refracted in different directions. This is problematic because the planned experiments involve driving specific atomic transitions, which again require specific polarisation. Birefringence in the glass cell makes it harder to find the correct polarisation. To measure the change of the polarisation a polariser was placed for the vacuum cell and an analyser behind the cell as shown in figure 3.8. The first polariser is set to achieve a parallel polarisation. The second polariser, the analyser, is set so that the polarisation axes are aligned or crossed. In practice, it is difficult to set the polarisation axes crossed to each other at an angle of 90°. Therefore, the waveplates were set so that the transmission was maximum T_{max} or minimum T_{min}. This means that no polarisation rotations can be measured with this method. However, any ellipticity introduced into the polarisation can be measured.

The polarisation which is altered after passing the cell can be measured with the polarisation extinction ratio (PER) [63]. The PER is given by

$$\text{PER} = \frac{T_{\text{min}}}{T_{\text{max}}}.$$

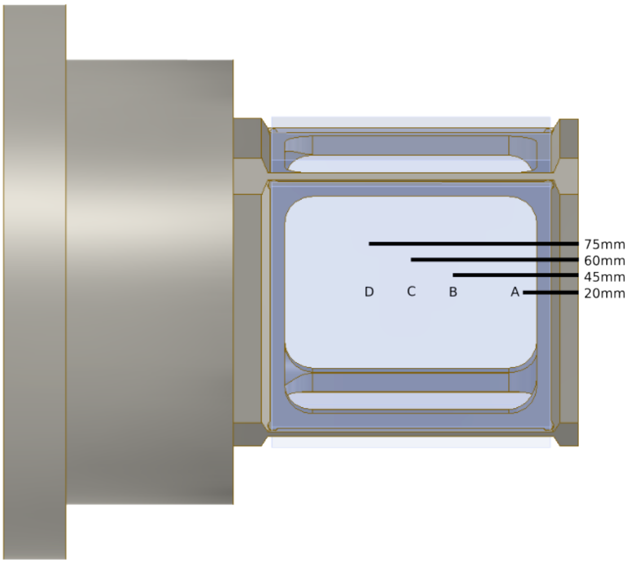

Figure 3.9: The positions of the measurement A, B, C and D are sketched on the homemade vacuum chamber

position	T_{min} [μW]	T_{max} [mW]	PER
without cell	1.98 ± 0.06	53.10 ± 0.16	$(3.7 \pm 0.2) \cdot 10^{-5}$
A	13.12 ± 0.04	49,84 ± 0.15	$(2.6 \pm 0.1) \cdot 10^{-4}$
B	2.38 ± 0.07	49,80 ± 0.15	$(4.8 \pm 0.2) \cdot 10^{-5}$
C	2.06 ± 0.06	49.96 ± 0.15	$(4.1 \pm 0.2) \cdot 10^{-5}$
D	2.11 ± 0.06	51.21 ± 0.15	$(4.1 \pm 0.2) \cdot 10^{-5}$

Table 3.2: The different measured T_{min} and T_{max} and calculated PER at different positions. Each transmission value was measured around 100 times and the mean value is given. The transmission errors are caused by the ±3% uncertainty of the used powermeter sensor [64] and the errors of the PER are calculated with the Gaussian error propagation.

When the polarisation changes, the PER increases. First the minimal transmission T_{min} and the maximal transmission T_{max} were measured without the vacuum cell. Afterwards, the vacuum chamber was placed between the polarisers and T_{min} and T_{max} were measured again. These measurements were repeated for different positions on the vacuum chamber window. The four measurement positions (A, B, C and D) are highlighted in figure 3.9. The different measured transmissions and the calculated PER are summarised in table 3.2.

For the measurement A, the PER is significantly higher than for the other measurements. Measurement A was taken at a distance of only 20 mm from the edge of the titanium frame. The higher PER fits with the expectations since the stress on the windows caused by the glueing the window to the

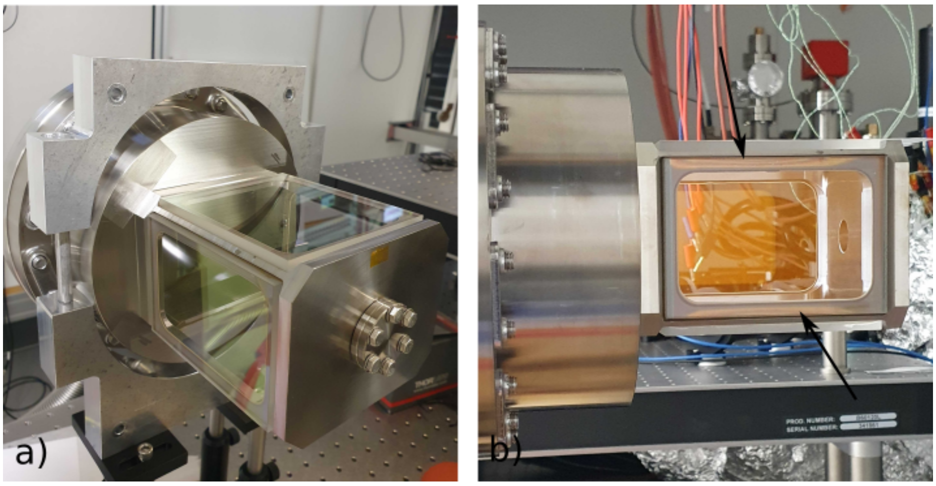

Figure 3.10: The vacuum chamber before a) and after bake-out b). Delaminations of the glue from the window can be seen after bake-out, indicated in b) by black arrows.

titanium frame and therefore the birefringence is expected to be strongest at the edges. The higher PER measured in position A in the experiment is not critical because the excitation lasers will pass the chamber at a distance of about 50 mm to the edge. This position would correspond to a position between measurement B and measurement C. The PER of measurements B, C and D are in the same regime as the PER without the cell. This shows that the stress on the window can be reduced by the design choice of using two materials with almost the same thermal coefficient, see section 3.1.2. Summarised the PER is sufficient for the experiment on the relevant position.

The cell was also analysed with regard to the vacuum in the science chamber. For this purpose, the cell was examined for failure of the glue bond, which could lead to leaks. A failure of the adhesion leads to delamination between the glue and the window or the titanium, which is noticeable by colour changes or a rainbow pattern. No delamination was noticed after curing and a pressure of 1.4×10^{-7} mbar was measured after 20 h pumping time at a molecularturbo pump, but some delamination can be found on the vacuum cell after a bake-out test, see figure 3.10. These delaminations are indicated by the rainbow pattern. These rainbow patterns can be caused by a gap between the glue and the window, which has a position-dependent size. This leads to position-dependent interference and a rainbow pattern in room light with different colours. The delaminations are not created after the curing and just appear after the bake-out. The reason for this behaviour could be the following: By curing the glue, the cell was placed in an oven without being attached to a vacuum pump. By the bake-out, the cell is connected to a molecularturbo pump. The bake-out construction is shown in figure 3.11. During the baked-out a temperature of 110 °C is achieved, which is higher than the glass transition temperature of the glue of 80 °C [48]. Therefore the glue is less solid. In addition, during the bake-out vacuum is inside the cell and this could cause some stress on the window. As a result, the window could lift from the glue. This behaviour is not noticed by curing the glue, which is done at a higher temperature (150 °C), because there no vacuum is inside the vacuum chamber and so no stress is on the windows.

Finally, the vacuum inside the science chamber was measured after the bake-out to check whether a

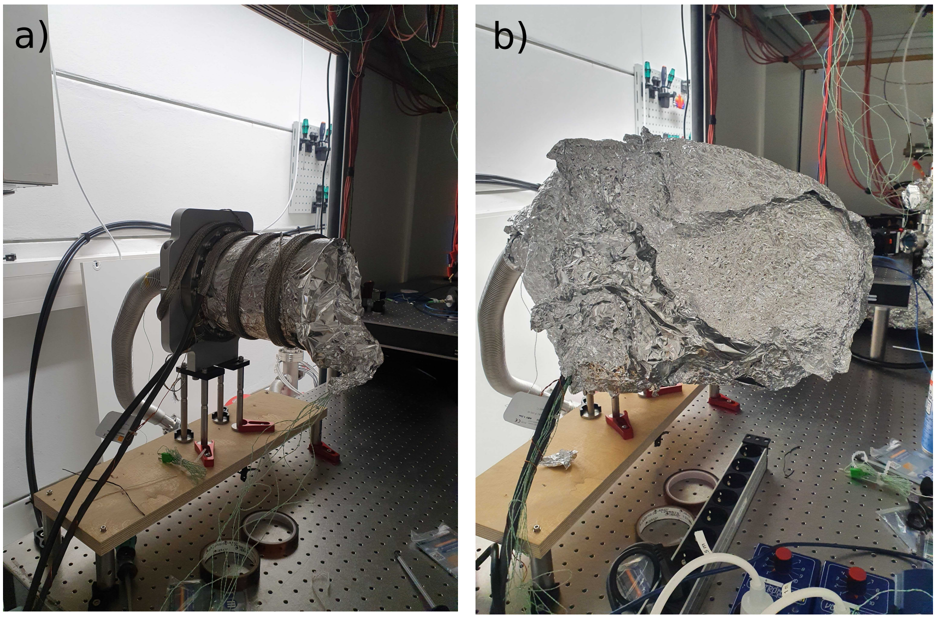

Figure 3.11: Construction for the test bake-out of the homemade science chamber. Temperature sensors are attached to the vacuum cell and a metal tube is fitted around the vacuum cell for protection. The tube is covered with aluminium foil to achieve a low gradient in the temperature along the science chamber and on the aluminium foil the heat wires are wrapped, see a). Afterwards, the construction is wrapped in some aluminium layers to achieve a more stable temperature environment by heating the cell. The entire construction is built on a wooden plate for temperature isolation from the table. The cell is connected to a turbo-pump.

leak had occurred. In general, bake-out is an important mechanism as the vacuum is limited by water at low pressure. In air, water can adhere to the material and adsorbed under vacuum. The adsorption rate can be increased if the material is heated. The pumping time can be shortened using the bake-out method [24]. The science chamber was heated with a temperature ramp from 5 °C/h to 110 °C.
To examine the vacuum in terms of quality a residual gas analyzer (RGA) was used to measure the partial pressures of the different elements in the residual gas in the vacuum chamber. Figure 3.12 shows a mass spectrum generated with an RGA on a Vacuum Pfeiffer turbomolecular pump connected to the vacuum cell. The mass spectrum shows that the vacuum is dominated by water and not by N_2 and O_2, which would mean that there is air in the cell [24]. For crosschecking, another method can be used, the helium leak test. This method is explained in section 3.1.2. The helium leak check method was used on the science chamber and the result is shown in figure 3.13 and it can be seen that there is no high increase of helium in the cell and therefore no leak.
Overall this vacuum cell meets the requirement in terms of pressure needed. For this reason, this vacuum cell was installed in the experimental setup instead of the first-generation vacuum cell. By using a NEG pump and ion pump, a pressure of 3×10^{-10} mbar is achieved at the NEG pump after 15 days. The defects could be avoided by glueing the second vacuum chamber in a clean environment, which could also have a positive effect on the adhesion between the titanium frame and the glue. Furthermore, with a slightly different design of the titanium frame, the glue could also bond from the side of the windows and not just from the bottom of the window, as was the case with the first chamber.

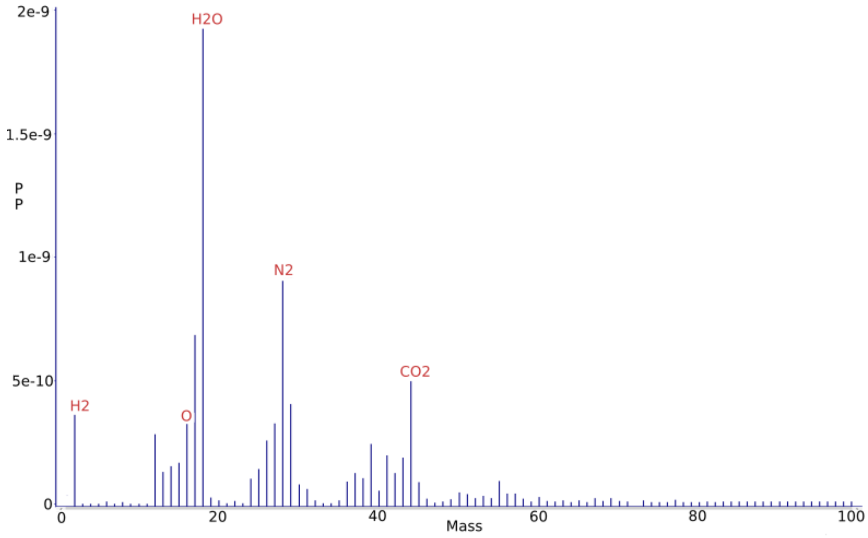

Figure 3.12: The result of a mass spectrum measurement of the vacuum inside the homemade vacuum cell after bake-out at 110 °C for five days. The partial pressure is plotted against the mass. The vacuum is dominated by water.

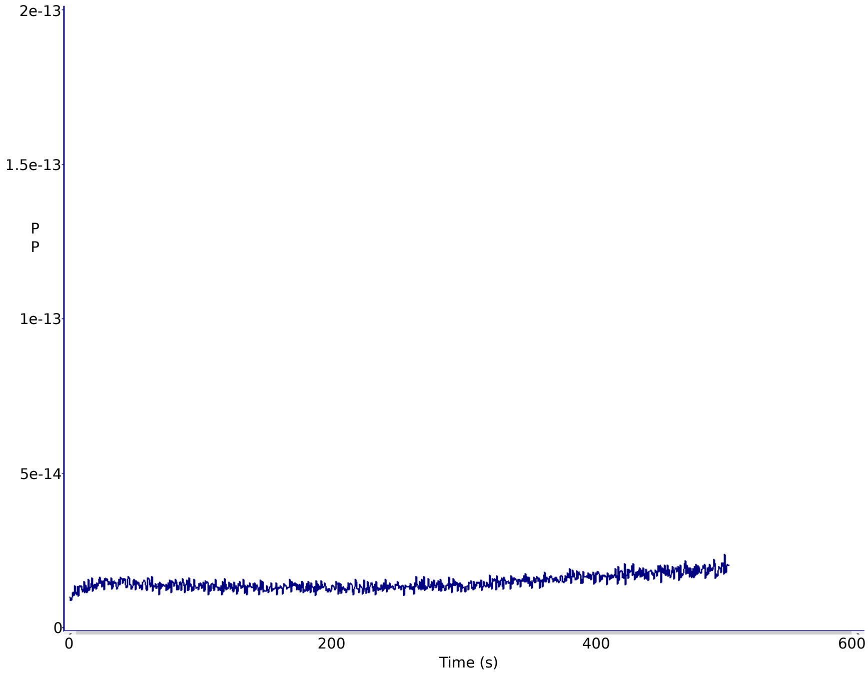

Figure 3.13: The result of a helium leak test around the homemade vacuum cell. The partial pressure of helium is plotted against time. By the helium leak test, every edge of the vacuum cell was checked. No high increase of a leak is found. The small increase of helium in this measurement is due to the characteristic of helium that it is a highly diffusible element and diffuses even through closed systems after a certain time.

3.2 Setup for Rydberg Atom Ionisation and Detection

The experimental setup is designed with a cryogenic environment in the SC. One of the advantages of a cryogenic environment is that ultra-high-vacuum (UHV) can be achieved without bake-out, a process that normally takes two to three weeks in this research group. With the cryostat, sample exchange is expected to take about one week. A cryogenic environment also increases the lifetime of the Rydberg states by reducing the black-body radiation induced decay, see section 2.2.1.
The cryostat will only be delivered after the end of this master thesis. Nevertheless, the cold atom preparation can be tested beforehand. The probe-control-setup for the Rydberg excitation and the design of the ion detection can be tested. As the probe-control setup will not be set up at the SC at the end of this master thesis, no data can be presented, but the working principle and the alignment of the ion detection parts can still be explained. This can be found in section 3.2. First, the theory of ionisation due to the electric field is introduced in section 3.2.1. Section 3.2.2 describes the design, alignment and process of the ionisation.

3.2.1 Ionisation of Rydberg Atoms

Rydberg atoms can be ionised even with relatively low electric fields.
Therefore, ionising the Rydberg atoms and detecting the remaining ion or electron can be used to measure Rydberg populations [65] [66]. Since the atoms are ionised at different electric field strengths depending on the principal quantum number n, the specific Rydberg state to which the atoms are excited can be measured. This can be done with a ramped electric field, where the atoms are ionised at different times and therefore the different Rydberg states can be distinguished by measuring time-dependent ion signals [66].
Accordingly, it is important to choose the electric field carefully in order to analyse the desired Rydberg state. For the first iteration of the experiment, a Rydberg state of $n = 68$ or $n = 85$ is aimed for. The ionisation energy for these two states is then calculated and the corresponding electric field is determined.

The ionisation energy is here calculated using a classical argument [67]. First, the outer classical turning point of the Rydberg electron is determined. In this argument, the atom is treated as a classical harmonic oscillator. The classical turning point is the position of an oscillator at which the kinetic energy is zero and the potential energy is equal to the total energy. Therefore, the energy can be calculated as follows

$$E_{\text{tot}} = E_{\text{pot}}, \tag{3.1}$$

where E_{tot} is the binding energy of the electron in the Rydberg state. E_{tot} [68] can also be expressed by

$$\begin{aligned}
E_{\text{tot}} &= -R \cdot h \cdot c \cdot \frac{1}{n^2} \\
&= -\frac{m_e e^4}{8 \cdot \epsilon_0^2 h^2} \cdot \frac{1}{n^2} \\
&\underset{\text{atomic units}}{\overset{\text{in}}{=}} -\frac{1 \cdot 1^4}{8 \cdot (\frac{1}{4\pi})^2 \cdot 1^2 (2\pi)^2} \cdot \frac{1}{n^2} \\
&= -\frac{1}{2n^2},
\end{aligned}$$

where R is the Rydberg constant, h is the Planck constant, m_e is the electron mass, e is the elementary charge and ϵ_0 is the vacuum permittivity.

The potential energy E_{pot} is determined using the radial part of the hydrogen wavefunction, since a Rydberg atom can be treated approximately like a hydrogen atom. The radial part of the wavefunction is used, because the potential depends on the radial distance only. The energy is calculated at the point where the kinetic energy is zero, therefore the radial wavefunction $R(r)$ is constant, which leads to

$$\begin{aligned}
E_{\text{pot}} &= \frac{l(l+1) \cdot \hbar^2}{2m_e r^2} - \frac{e^2}{4\pi\epsilon_0 r} \\
&\underset{\text{atomic units}}{\overset{\text{in}}{=}} \frac{l(l+1)}{2r^2} - \frac{1}{r}.
\end{aligned}$$

Using equation 3.1, this results in

$$-\frac{1}{2n^2} = \frac{l(l+1)}{2r^2} - \frac{1}{r}. \tag{3.2}$$

To determine the classical turning point, equation 3.2 is solved for r, which gives the expression of

$$r_{\text{out/in}} = n^2 \pm \sqrt{n^4 - n^2 \cdot l(l+1)}. \tag{3.3}$$

For the ionisation an additional electric field F_{add} is applied, which results in a Stark shift added on the Coulomb potential

$$V = -\frac{1}{r} + F_{\text{add}} \cdot r.$$

The potential V is maximal at

$$r_{\max} = \frac{1}{\sqrt{F_{\text{add}}}}. \tag{3.4}$$

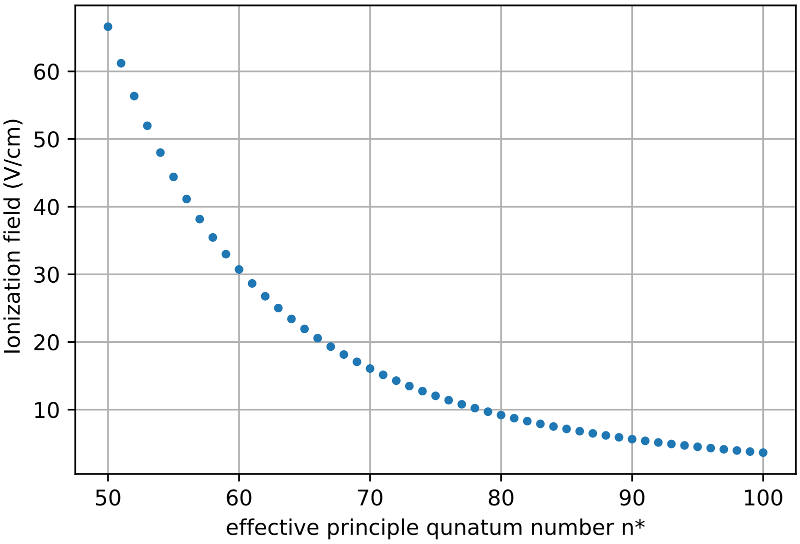

Figure 3.14: The ionisation field dependent of the effective principal quantum number.

The atom is ionised, when the classical outer turning point of the electron is outside of the maximum of the potential. Using equation 3.3 and 3.4 the electric field for ionisation is given at

$$F_{\text{ionisation}} = \frac{1}{(n^2 + \sqrt{n^4 - l(l+1)})^2}.$$

For S-states (l=0) and using the international system of units (S.I units) the electric field for ionisation $F_{\text{ionisation}}$ results in

$$\begin{aligned} |F_{\text{ionisation}}| &= \frac{1}{n^{*4}} \cdot \frac{\pi \epsilon_0 \mathrm{R}_{\mathrm{y}}^2}{e^3} \\ &= \frac{1}{n^{*4}} \cdot 3.2138 \times 10^8 \,\mathrm{V\,cm^{-1}}, \end{aligned}$$

where $\mathrm{R_y}$ is the modified Rydberg constant and n^* is the effective principle quantum number $n^* = n - \delta_{nlj}$. This dependence is visualised in figure 3.14. The quantum defect δ_{nlj} takes into account that the electron interacts with just a fraction of the atom core due to the shielding from the remaining electrons around the core. The quantum defect for ^{87}Rb S-states is 3.131 180 7(8) [69]. This leads for $n = 68$ and $n = 85$ to a ionisation electric field $F_{\text{ionisation}}$ of

$$\begin{aligned} |F_{\text{ionisation}}(n = 68)| &= 18.1488 \,\mathrm{V\,cm^{-1}} \\ |F_{\text{ionisation}}(n = 85)| &= 7.1535 \,\mathrm{V\,cm^{-1}}. \end{aligned}$$

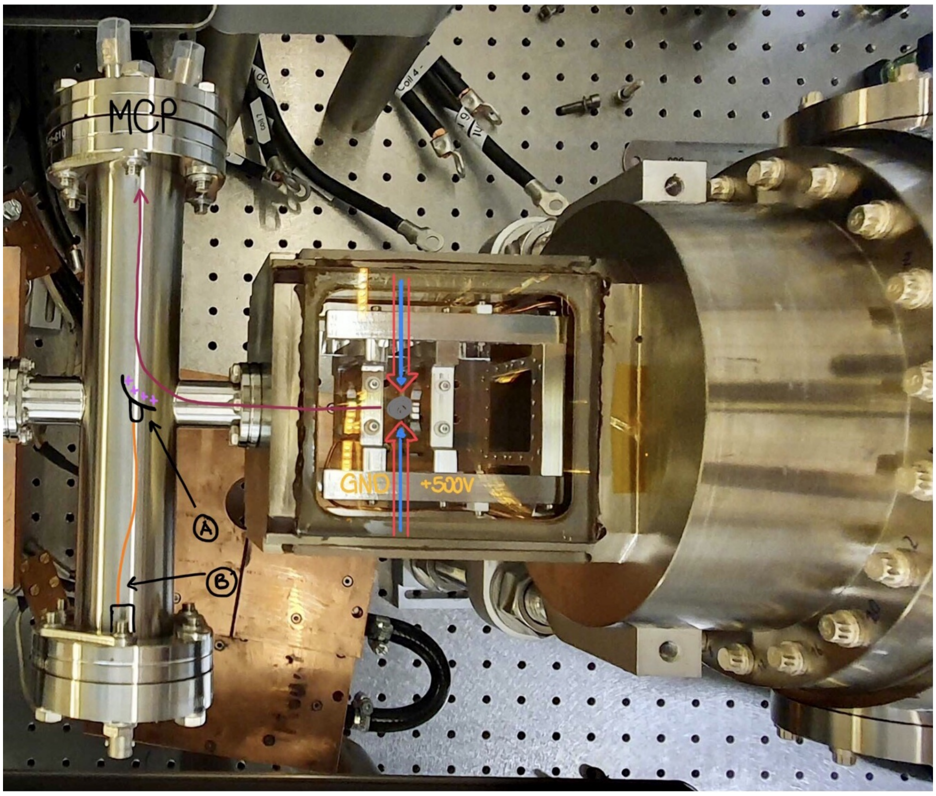

Figure 3.15: The entire ion detection pathway as a sketch. The rubidium atoms, shown as a grey dot, are excited to the Rydberg state with a two-photon excitation, as indicated by the red and blue arrows. By applying a positive voltage of, for example, 500V to electrode 1 (yellow number), the Rydberg atom is ionised and pushed to the deflection electrode, labelled with (A). The trajectory of this process is marked by the dark red arrows. The deflection electrode also has a positive voltage, but a lower one than electrode 1 and deflects the ion to the MCP (Micro-Channel-Plate), shown with purple plus and dark red arrow. The deflection electrode is connected to a feedthrough via a Kapton wire, labelled with (B). The ion is detected at the MCP.

3.2.2 Assembly of the Rydberg Detection Setup

In this section, the design and alignment of the ion detection are described. The whole ion detection path is shown in figure 3.15 and can be separated into three main parts. The ionisation of the Rydberg atoms, the ion deflection to the MCP (Micro-Channel-Plate) and the detection of the ions at the MCP.

The first step in the ion or Rydberg atom detection process is the ionisation of the Rydberg atoms. The ^{87}Rb atoms are initially excited with the two-photon excitation to a Rydberg state, as discussed in the previous section. After the quantum optics experiments, that are planned for the experiment, the remaining Rydberg atoms are ionised by an electric field, see also in section 3.2.1. Figure 3.16 shows a sketch of the ionisation process. A positive voltage is applied to electrode 1, and electrode 2 is connected to the ground. This leads to an electric field across the region where the Rydberg atoms are located. After the ionisation the atomic nucleus is positively charged and is pushed to the ion deflection of the highly positive electrode 1.
Figure 3.17 shows the design of the electrodes. The electrodes are not only used for ionisation but also

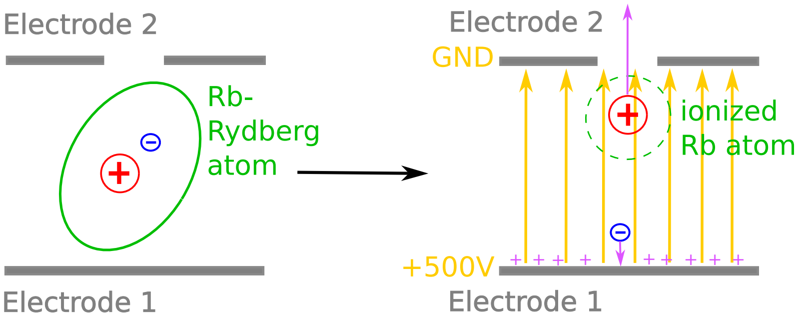

Figure 3.16: A sketch of the working principle of ionisation. First, the rubidium atom is excited to a Rydberg state and no voltage is applied to the electrodes. In the second step, a voltage of, for example, +500 V is applied to electrode 1 while electrode 2 is connected to ground. This leads to an electric field, indicated by the yellow arrows. The electron is attracted by the positive voltage and the positive ion is pushed away.

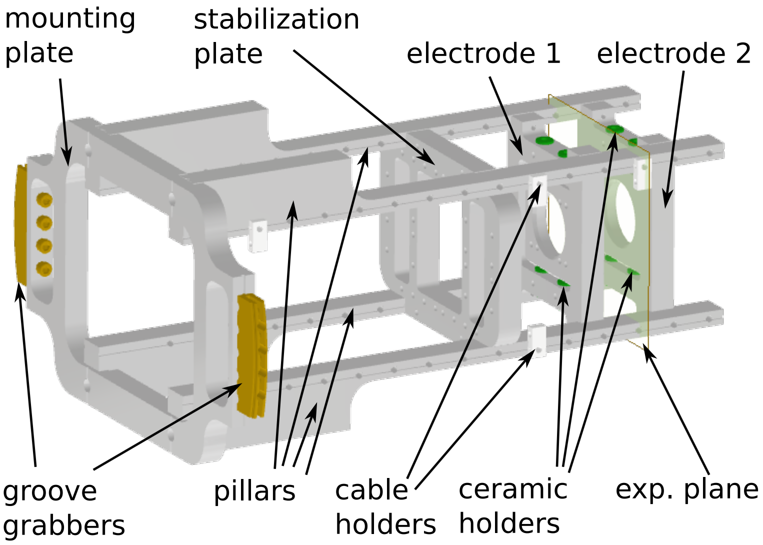

Figure 3.17: The inner assembly is shown as a CAD sketch. The different parts are labelled.

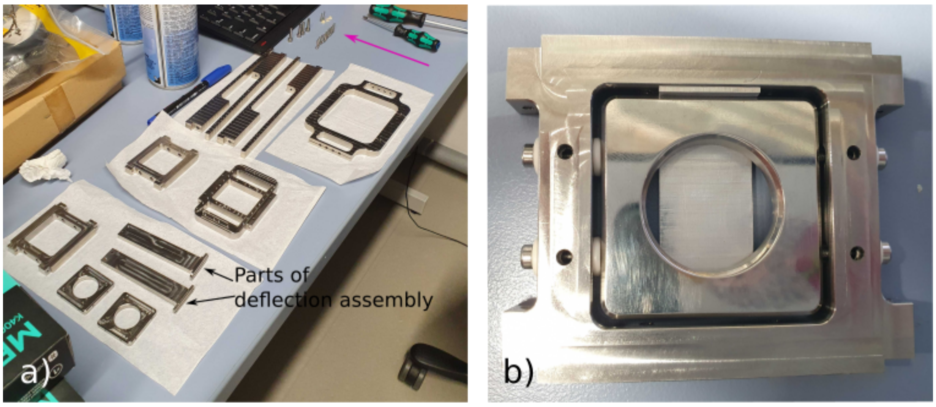

Figure 3.18: The unmounted inner assembly. In a) the entire unmounted inner assembly is shown. Also, two parts of the ion deflection assembly are there, labelled with a black arrow. The purple arrow indicates the required screws and ceramic holders. In b) the alignment of the electrode is shown. With an aluminium L-shape tool, the alignment in the horizontal plane is done. On the left side, the ceramic holders are missing to avoid mechanical stress on the ceramic holders. To the polished side of the electrode lays above.

for applying a constant electric field to push the ion to the deflection electrode. This first-generation design does not have an integrated field compensation as the setup is only temporarily used for ion detection until the cryostat is connected to the experimental setup. The sides of the two electrodes facing each other are polished to obtain a more homogeneous electric field. The electrodes are spaced 20 mm apart and are isolated from the entire inner assembly by ceramic mounts. The third steel plate serves to stabilize the inner assembly. Ceramic cable holders for the Kapton wire are located on the pillar of the inner assembly.

Figure 3.18 shows the components of the inner assembly. All non-commercial parts are made by the house workshop from grade 316L (A4) stainless steel. The screws are made of grade 304 (A2) stainless steel. The entire setting up of the inner assembly has to be done under conditions which fit the requirements of vacuum cleanliness. To avoid unforeseen complications during installation, the inner assembly construction was tested beforehand under normal conditions. In figure 3.18 a) the different unmounted parts are shown. By testing the assembly and the alignment of the inner assembly, it was noticed that the alignment of the electrodes has to be done with an extra tool, shown in figure 3.18 b). With an aluminium L-shape tool, the distance between the electrode and the mount of the electrode can be fixed when the electrode is screwed on the mount and a precision of around 0.01 mm is achieved. Also, as it can be seen in figure 3.18 b) on the right side the ceramic holders between the electrode and mount are missing. This is the case because with ceramic holders on both sides, the space was not large enough and the ceramic holder could get some mechanical stress, which could crack the ceramic holders and thereby contaminate the vacuum. By tightening the screws it was also taken care to not give stress on ceramic holders.

After the test assembly under normal conditions, the components were cleaned for vacuum and assembled a second time onto the octagon via the pillars [42], which are mounted on a mounting plate which is screwed onto the octagon using groove grabbers[7]. The electrodes are connected with

---

[7] 8.00" groove grabbers from Kimball Physics [70]

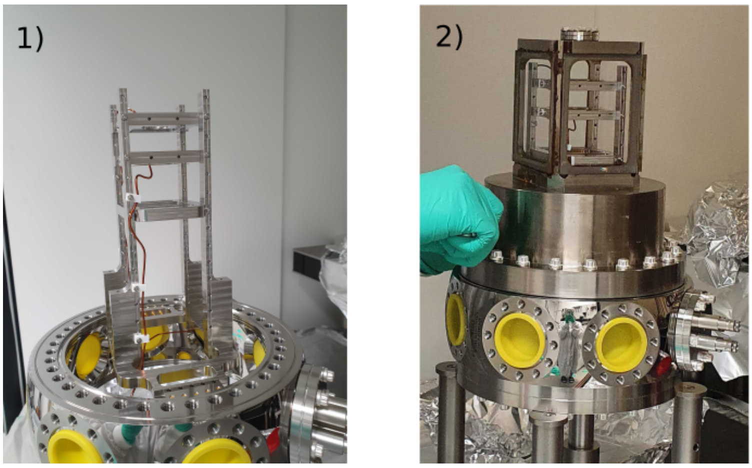

Figure 3.19: The design of the inner assembly is shown physically. In 1) the inner assembly is mounted on the octagon and the wire to the electrode 1 is connected. In 2) the homemade vacuum cell is mounted above the inner assembly and on the octagon. On the right side in 2) the SHV (safe high voltage) feedthrough to supplied with power the electrodes from outside are mounted on the octagon. The yellow plastic caps on the octagon are for safety and were removed by assembling the entire setup.

Kapton wire[8] to the SHV (safe high voltage) feedthroughs[9] on the octagon, see figure 3.19. When mounting the inner assembly on the octagon, care is taken to ensure that there is no tilt angle between the octagon and the inner assembly and therefore the electrodes are perpendicular to the atom transport axis. With this alignment, the atoms should have a straight path for the ion deflection.
With the explained electrode geometry the voltage U experienced by the Rydberg atoms can be determined for $n = 68$ and $n = 85$ by using a Comsol simulation, created by Hannes Busche. This simulation was modified for the two specific cases which leads to

$$\begin{aligned} U(n = 68) &= 47.2\,\mathrm{V} \\ U(n = 85) &= 18.6\,\mathrm{V}. \end{aligned}$$

The maximum applied voltage is 500 V, which leads to an electric field of $192\,\mathrm{V\,cm^{-1}}$. The minimum principal quantum number n that can be ionised with the setup is therefore

$$\begin{aligned} n &= \left(\frac{3.2138\times10^{8}\,\mathrm{V\,cm^{-1}}}{192\,\mathrm{V\,cm^{-1}}}\right)^{\frac{1}{4}} + 3.13118 = 39.0997 \\ n_{\text{minimal}} &= 40. \end{aligned}$$

After the Rydberg atoms have been ionised, the ions will be accelerated through the connecting tube between the MOT and the science chamber, where the ion deflection electrode is located. This electrode will be kept at a lower positive voltage than electrode 1. The potential is therefore for the

---

[8] Kapton wire with OD 1.4 mm and conductor 1.3 mm from Allectra [71]

[9] SHV CF40 feedthroughs from Allectra [44]

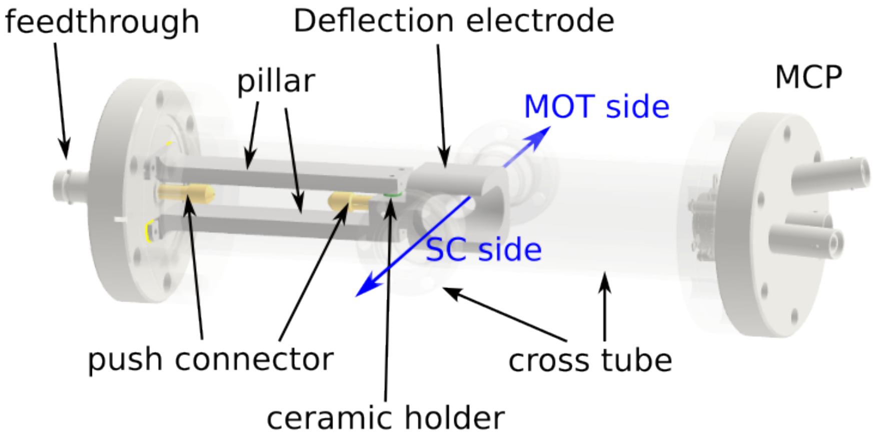

Figure 3.20: A CAD sketch of the ion deflection and MCP part. The different components and the adjacent areas of the experimental system are labelled.

ions repulsive and the ions are slowed down. Furthermore, the ions are pushed in a perpendicular direction to the incoming direction regarding the shape of the electrode. The ions are deflected to the MCP.

The design of the ion deflection is shown in figure 3.20.

The pillars and the deflection electrode are made by the house workshop from grade 316L (A4) stainless steel. The deflection electrode is isolated from the remaining assembly with ceramic holders and screwed onto pillars, which are mounted with vented screws on a feedthrough[10]. The feedthrough is connected to the deflection electrode via Kapton wires and push-on connectors[11] and is supplied with power from the outside. The entire deflection assembly is inside a cross tube.

The micro channel plate (MCP)[12] is mounted on the other end of the cross tube. The MCP is connected from the outside. Individual ions can be measured with the MCP. When an ion hits the effective surface of the MCP, an electron is emitted. The electron is accelerated due to a voltage, which is applied between the input and the output sides of the MCP. Due to the shape of the channel, the accelerated electrons collide again with the channel material and further electrons are emitted. This process is repeated so that at the output the one electron has been multiplied by secondary emission to form a large number of electrons. This signal can then be read out.

With this ion detection assembly, it should be possible to measure an ion signal and Rydberg atoms, respectively at room temperature. A simulated trajectory of the ions is shown in figure 3.21, which was designed by Hannes Busche using Comsol.

---

[10] BNC 40CF feedthrough from Allectra [72]

[11] Power push on connectors from Allectra [73]

[12] MCP F4655-11 from Hamamatsu is mounted on a 40CF flange[74]

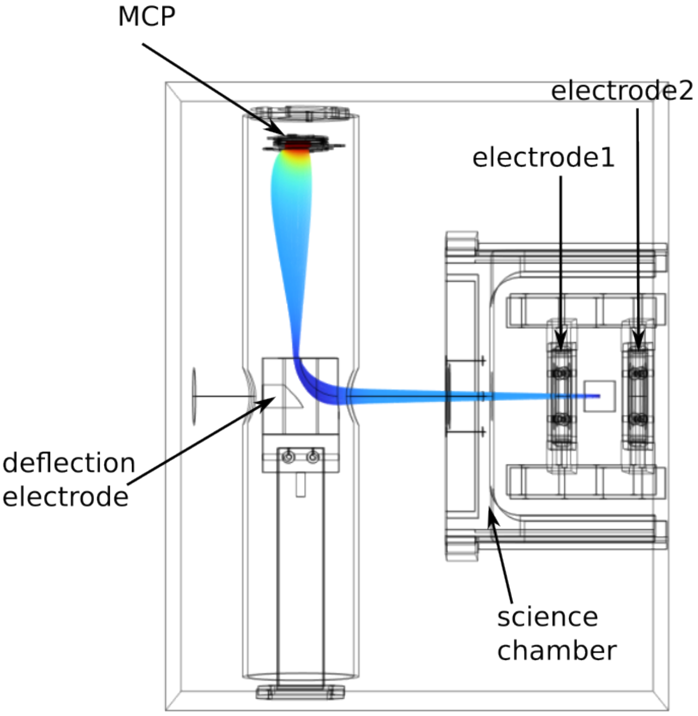

Figure 3.21: The ion trajectory in the ion detection setup at room temperature is shown. The voltage of electrode 1 is 300 V and of electrode 2 is the voltage 0 V. On the deflection electrode is a voltage of 108 V applied and on the MCP front plate a voltage of −1 500 V.

CHAPTER 4

Cold Atom Preparation and Imaging

The rubidium atoms are prepared in the MOT chamber from a background gas at room temperature, see chapter 2. After the preparation in the room temperature MOT chamber, the atoms are transported into the science chamber (SC) in a cryogenic environment using magnetic fields. In order to check the efficiency of the magnetic transport, an absorption imaging system is set up at the SC. The absorption imaging system can be used to determine the number of atoms as well as the temperature and the position to which the atoms are transported. This setup and the characterisation of the imaging setup are described in detail in section 4.1. Section 4.2 describes in detail the working principle of the magnetic transport and how it is assembled. Finally, one transport sequence will be explained briefly.

4.1 Imaging in the Science Chamber

Imaging in the science chamber is primarily used to check the efficiency of the magnetic transport. For this purpose, absorption imaging is set up to verify the number and the temperature as well as the position of the transported atoms inside the SC. To determine the position of the atoms, two imaging setups are built perpendicular to each other and to the magnetic transport. The setup that images along the horizontal (x) axis is referred to as the horizontal setup and the setup along the vertical axis (z) as the vertical imaging setup. With these two setups, it is possible to visualise the position of the atoms in three dimensions. The position of the atoms must be correct because the excitation lasers, also known as the probe-control-setup which will replace the horizontal imaging, can only excite the atoms with a high efficiency if the lasers hit the atoms accurately. In addition, the atoms are trapped in a magnetic trap that is positioned relative to the axis of the probe-control-setup.
Section 4.1.1 briefly explains the working principle of the absorption imaging. The two absorption imaging setups are described in section 4.1.2. Since the horizontal setup will be replaced by the probe-control-setup, the focus is set on the vertical setup in the description of the setups as well as in the characterisation of the imaging setup, which is explained in section 4.1.3.

4.1.1 Absorption Imaging

In this subsection, the absorption imaging is only explained very briefly, further information can be found in [75] or [76], for example.
Absorption imaging is a powerful technique in which the absorption of laser light is imaged and this

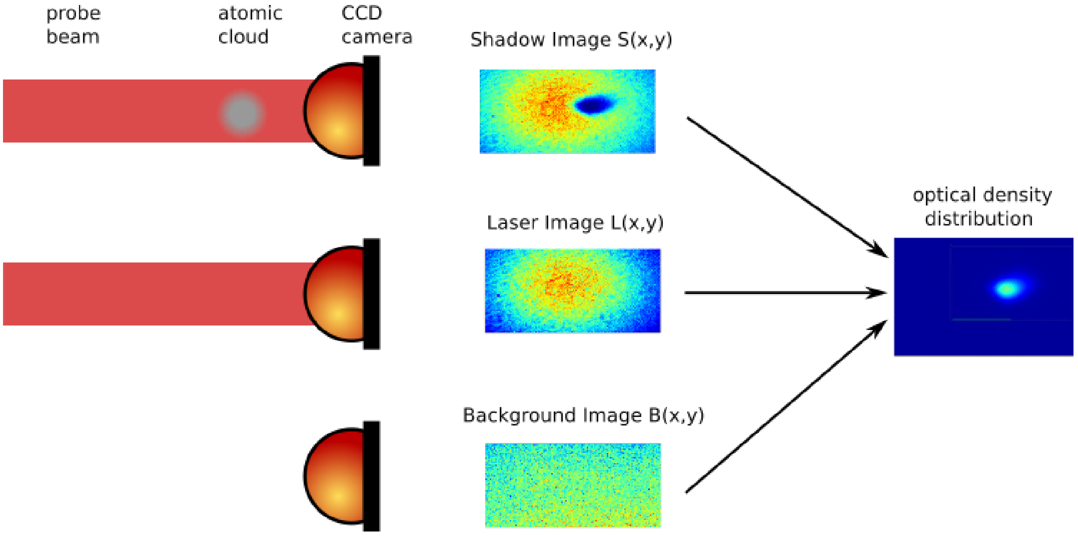

Figure 4.1: In this figure the working principle of the absorption imaging is shown. For the absorption imaging, three images are taken. The first image is the so-called shadow image S(x,y) where a laser which is resonant to the atomic cloud passes the atomic cloud and gets partially absorbed. The shadow of the atomic cloud and the laser are imaged on a CCD camera. Afterwards, only the laser is imaged and therefore the image is called laser image L(x,y). The last image is the background image. In this image, the background stray light and the dark current, which means the noise only, are measured.

absorption is used, for example, to obtain information about the position and the number of the atoms in an atomic cloud. The procedure of the absorption imaging is sketched in figure 4.1.

For the absorption imaging three images are required. In the first image, a laser passes through an atomic cloud with which the laser is in resonance. Depending on the atomic density, the atomic cloud absorbs more or less of the light and casts a shadow in the propagation direction. The beam and the shadow of the atomic cloud are then imaged on a CCD camera. The taken image is the so-called shadow image $S(x,y)$. A second image, the so-called laser image $L(x,y)$, is taken without atoms. In this image, only the beam is imaged on the CCD camera. The third image only measures the background stray light and the dark current of the CCD camera, which means the noise. Therefore this third image is called the background image $B(x,y)$.
The background is subtracted from the shadow image and the laser image. With these two intensity distributions, and under consideration of the Beer-Lambert law [46] it is possible to determine the column density $n(x,y)$

$$n(x,y) = -\ln\left(\frac{S(x,y) - B(x,y)}{L(x,y) - B(x,y)}\right) \cdot \frac{1}{\sigma_0},$$

with $\sigma_0 = \frac{3\lambda}{2\pi}$, which is the resonant cross section [76].
By integrating over the column density $n(x,y)$ the atomic number N_{atom} is calculated [75]. This

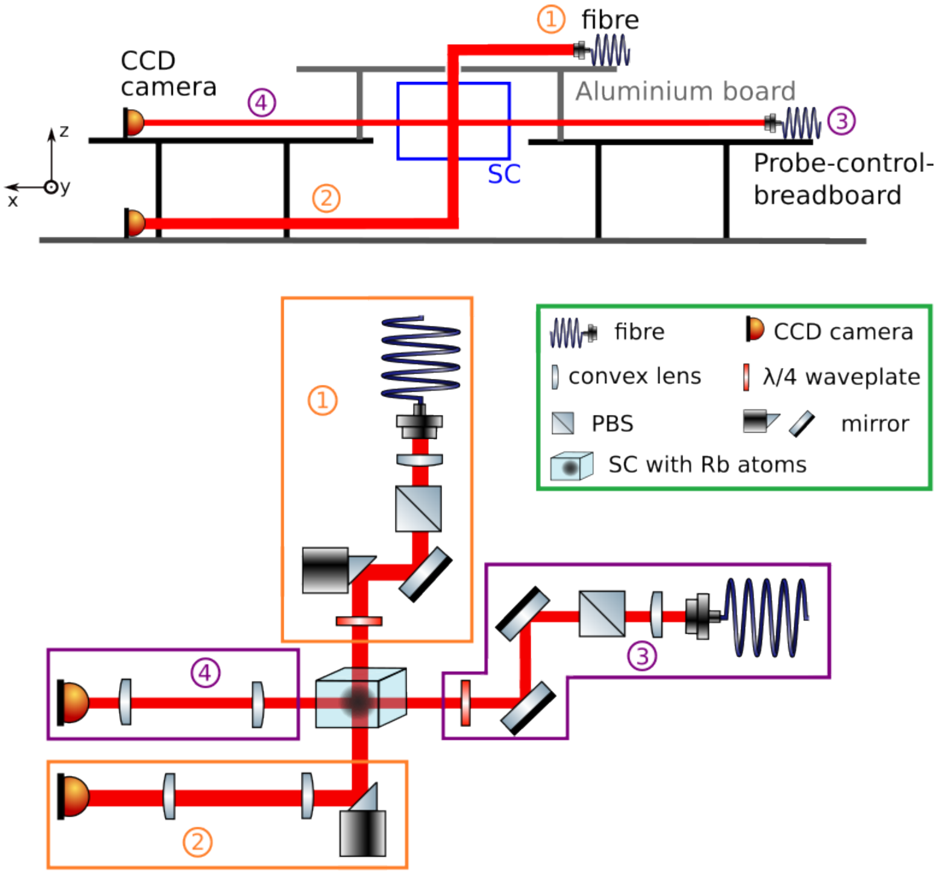

Figure 4.2: The combined vertical and horizontal absorption imaging setup on different tables. With this setup, the position of the trapped atoms in the science chamber in three dimensions can be detected. At the top, the construction of the tables is sketched from the front view. Below the combined absorption imaging setup is shown. In the orange box, the vertical setup is sketched and in the purple box the horizontal setup. The numbers give the positions of the setup parts on the probe-control-breadboard, the aluminium board and the experimental table, respectively.

results in the equation of

$$N_{\text{atom}} = \int_{-\infty}^{\infty} \int_{-\infty}^{\infty} n(x, y)\, dx\, dy \cdot f^2, \tag{4.1}$$

where f is the factor to convert the pixel into meters, in this experiment: $f^2 = 6.45\,\mu\text{m}^2 \cdot 2$ [77].

4.1.2 Setup

This subsection describes the two absorption imaging setups. At first, the vertical and then the horizontal imaging setup is explained. The combined setup of the two imaging systems is shown in figure 4.2. The laser used for the two imaging setups is described in chapter 5.
In the following the vertical absorption imaging is described.

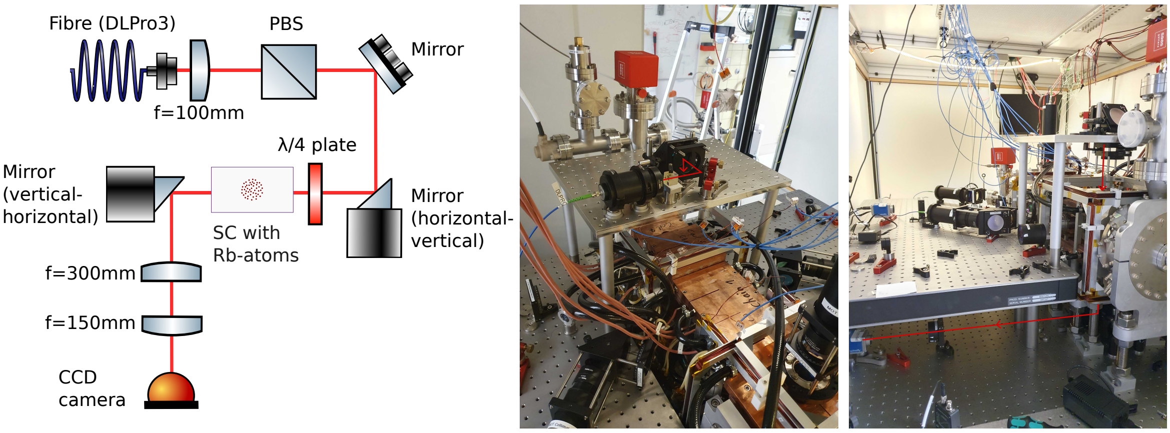

Figure 4.3: The vertical imaging setup. On the left, a sketch of the vertical setup is shown. In the middle and right picture, the physical vertical imaging setup can be seen. With the lens behind the fibre, the beam is collimated and the PBS removes the unwanted polarisation. The horizontal-vertical-mirror reflects the beam from the horizontal direction to the vertical direction. The following $\lambda/4$-waveplate converts the linear polarisation to a circular polarisation. The beam can then be absorbed by rubidium atoms in the SC. Afterwards, the vertical beam is reflected with the vertical-horizontal-mirror in the horizontal direction again. A telescope is built in front of the camera with a $f = 300$ mm and $f = 150$ mm achromatic planoconvex lens, which results in a magnification factor of 0.5.

The sketch of the vertical setup is shown in figures 4.2 and 4.3. The first part of the setup is built onto an optical breadboard of aluminium, which is mounted on the optical breadboards in such a way that the board is above the SC, see figure 4.3. The board is made by the IAP mechanical workshop and the design was chosen such that a 50 mm diameter hole in the board is above the vacuum cell. The accuracy of the position of the hole is ensured by screwing the legs of the aluminium board directly onto the optical breadboards, which in return are correctly aligned to the vacuum cell.

For the imaging a diode laser DLPro3 from Toptica is used. This laser is discussed in chapter 5. The light from that laser is fibre coupled on the laser table and guided to the imaging setup. The single mode fibre[1] is polarisation maintaining. To collimate the beam after the fibre an achromatic lens[2] with a focus of $f_{\text{fibre,v}} = 100$ mm is placed at a distance of 100 mm away from the fibre. The calculated beam diameter is 18.7 mm[3] . A polarising beamsplitter (PBS) is mounted behind the achromatic lens. This is done to control the polarisation of the beam, because the polarisation may change by passing the fibre from the laser table to the experiment even though a polarisation-maintaining fibre has been used. These changes can be caused by temperature fluctuations. The PBS only transmits a desired linear polarisation. Behind the PBS the beam is reflected from one mirror to another mirror. The second mirror is placed above the hole in the table and reflects the beam from the horizontal direction to the vertical direction, and is therefore called the horizontal-vertical-mirror. Behind the horizontal-vertical mirror, a $\lambda/4$-waveplate [82] is attached to the backside of the aluminium

---

[1] polarisation maintaining single mode fibre from Thorlabs, $\lambda = 780$ nm (P3-780PM-FC-10) [78]

[2] two inch archomatic doublet from Thorlabs, $f = 100$ mm [79]

[3] Note this a $1/e^2$ diameter, calculated with $d = 2 \cdot \omega_0 = \frac{\lambda \cdot f}{\pi \cdot (MFD/2)}$, Mode field diameter $(MFD) = (5.3 \pm 1.0)\,\mu$m [80] [81]

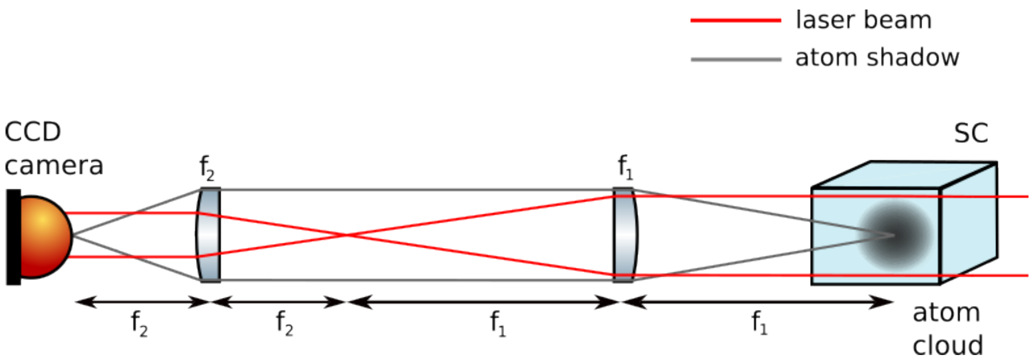

Figure 4.4: The optical path of the laser beam and atom shadow in the vertical and horizontal absorption imaging. The laser beam is indicated by the red line and the atom shadow by the grey line. The first lens is placed at a distance to the atom cloud which is equal to the focal length of the first lens. The distance between both lenses is $f_1 + f_2$. The CCD camera is placed in the focus of the second lens.

breadboard. The $\lambda/4$-waveplate is mounted at this position because the polarisation must be set precisely and the polarisation can be changed uncontrollably in the case of reflection. With the $\lambda/4$-waveplate the linear polarisation is converted into σ^+ circular polarisation. Next, the circularly polarized beam goes through the SC and is reflected at the mirror behind the SC from the vertical direction to the horizontal direction. The mirror is therefore referred to as a vertical-horizontal mirror. The light from the beam is detected in the horizontal plane on a charged coupled device (CCD) camera[4]. In front of the CCD camera, a telescope is set up with a magnification factor of 0.5 with two achromatic convex lenses of a focal lengths of $f_{1,\mathrm{v}} = 300\,\mathrm{mm}$[5] and $f_{2,\mathrm{h}} = 150\,\mathrm{mm}$[6], respectively. The trapped atoms inside the SC have a distance to the first lens that corresponds to the focal length of the first lens. The CCD camera is located at a distance of 150 mm from the second lens. If atoms are inside the SC the beam is absorbed. The shadow of the atoms is magnified by a factor of 0.5 on the camera with this configuration of the two lenses and the position of the CCD camera. The CCD camera has a pixel size of 6.45 µm [77]. The optical path of the beam and the atom shadow are shown in figure 4.4.

The horizontal setup is shown in figure 4.5 and is based on the same principle as the vertical setup. A lens with $f_{\mathrm{fibre,h}} = 60\,\mathrm{mm}$[7] is placed behind the fibre to collimate the beam, resulting in a calculated beam diameter of 11.2 mm[8]. The following PBS removes the unwanted polarisation component. Two mirrors are then installed to align the beam with correct angles with respect to the SC and also to the axis of the planned probe-control-setup. Behind the two mirrors a $\lambda/4$-waveplate is mounted to convert the linear polarisation into a σ^+ circular polarisation. The beam then passes through the chamber. Behind the SC is a telescope with two lenses that has a magnification factor of 0.4. The

---

[4] pco.pixelfly usb from Excelitas [77]

[5] two inch archomatic doublet, $f = 300\,\mathrm{mm}$ [83]

[6] two inch archomatic doublet, $f = 150\,\mathrm{mm}$ [84]

[7] one inch archomatic doublet from Thorlabs, $f = 60\,\mathrm{mm}$ [85]

[8] Note this a $1/e^2$ diameter, calculated with $d = 2 \cdot \omega_0 = \frac{\lambda \cdot f}{\pi \cdot (MFD/2)}$, $MFD = (5.3 \pm 1.0)\,\mu\mathrm{m}$ [80] [81]

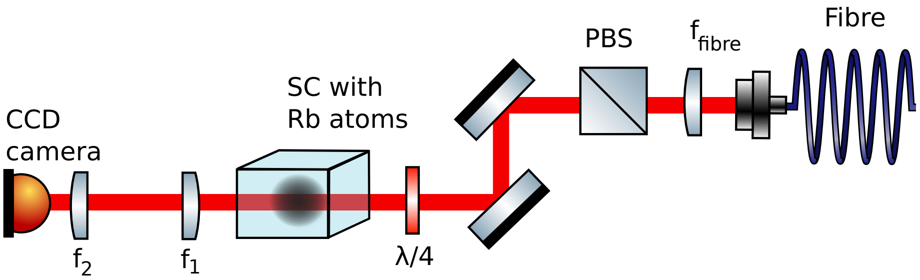

Figure 4.5: From right to left the horizontal absorption imaging setup. The lens behind the fibre collimates the beam and the PBS removes unwanted polarisations. With the two mirrors, the beam is aligned relative to the science chamber and on the probe-control-setup-axis. In front of the CCD camera, a telescope is built with a $f = 250$ mm and $f = 100$ mm achromatic planoconvex lens, which results in a magnification factor of 0.4.

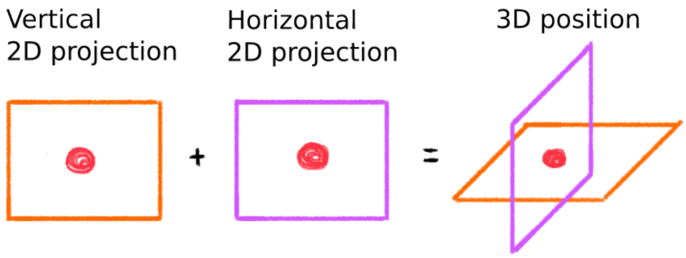

Figure 4.6: A sketch of two 2D projections which, when superimposed at right angles, lead to a 3D position determination.

two achromatic convex lenses have a focal length of $f_{1,\mathrm{h}} = 250\,\mathrm{mm}$[9] and $f_{2,\mathrm{h}} = 100\,\mathrm{mm}$[10]. The CCD camera is positioned at a distance of 100 mm from the second lens. The model of the CCD camera is the same as for the vertical imaging.

By setting up both imaging setups around the SC, it is now possible to verify the position of the trapped atoms in the SC in three dimensions, see figure 4.6.

4.1.3 Characterisation

The purpose of the absorption imaging is to determine the position and the atom number of the atom cloud. Therefore the stability and noise of the absorption imaging must be characterised beforehand in order to know how reliable the measurements are. This characterisation is described in the following.

When the horizontal imaging was first set up through the science chamber, an unexpected beam pattern was noticed on the CCD camera. The CCD camera did not measure one Gaussian beam but an interference pattern, see figure 4.7. This could be caused by the interference resulting of a small angle between the two vacuum cell windows at the horizontal axis, which acts like a cavity. This behaviour was not noticed for the vertical imaging.

Since the horizontal imaging setup will be replaced with the probe-control-setup and because the beam

---

[9] two inch archomatic doublet from Thorlabs, $f = 250$ nm [86]

[10] one inch archomatic doublet from Thorlabs, $f = 100$ nm [87]

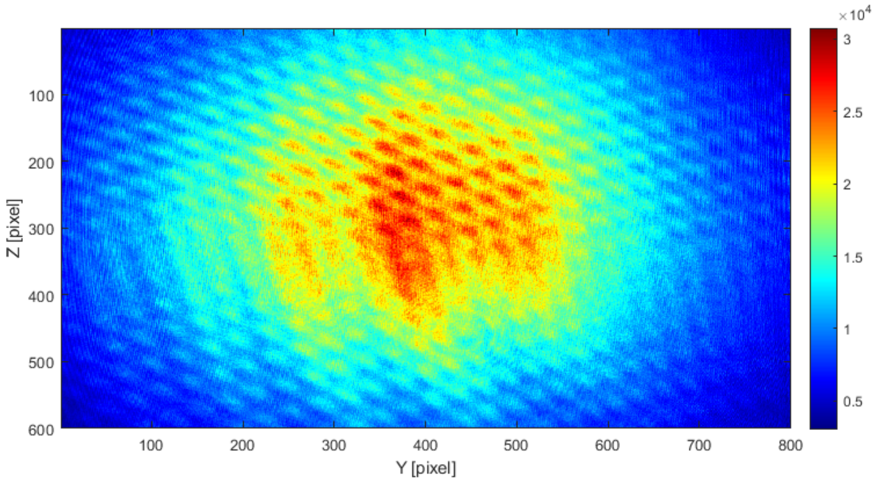

Figure 4.7: A interference pattern is shown. This interference pattern can be caused by a small angle between both science chamber windows on the horizontal axis and so cavity behaviour seems to be created.

for the vertical imaging is not visibly distorted by the science chamber, the focus of the characterisation was set on the vertical imaging.

To ensure reliable atom number measurements the noise has to be constant and small over a large time as well as for short times. For the noise measurement, no atoms were in the SC. First, the noise of a long time scale is analysed. The noise was measured over 12 hours and the counts of each image were summed over all pixels for each measurement. The measurement is shown in figure 4.8. The noise of the three images seems to be stable over a long time. But when the ratio is taken from the shadow image and the laser image to analyse the stabilisation over short times, there is an offset. A value of one would be expected for the ratio when both images would have the same amount of counts, which would mean that the intensity would not change significantly on short time scales. But the mean distribution of the ratio is not centred around one but is shifted to 1.01, see figure 4.10a). It seems therefore that the shadow images, the first images in the sequence, often have a higher intensity than the laser images, the second images in the sequence. This could be caused by a heating effect of the AOM (acousto-optic modulator) and therefore a time dependent intensity change or a non-overlapping AOM signal and exposure signal of the camera..

To verify that the offset is not caused by the timing of the imaging light on-time and the camera exposure signal these two signals were compared to each other. For the imaging light on-time, the beam was measured on a photodiode and the signal was displayed on an oscilloscope. This measurement is given by the yellow line in figure 4.9. The exposure duration time of the camera is given by the green line. Both signals overlap perfectly, which means that this can not have caused the problem.

To investigate the heating effect of the AOMs the time between taking the three images was varied. In figure 4.10 the ratio of the shadow image and the laser images is computed for times of 70 ms, 100 ms and 400 ms, between taking the images. With a larger time between taking the images the mean value of the ratio approaches the value 1. It seems that the heating effect of the AOM caused different intensities for the shadow image and the laser image. Since 400 ms are too large for the time between images and the offset for 100 ms is not significantly large, the time between taking the images is set to 100 ms.

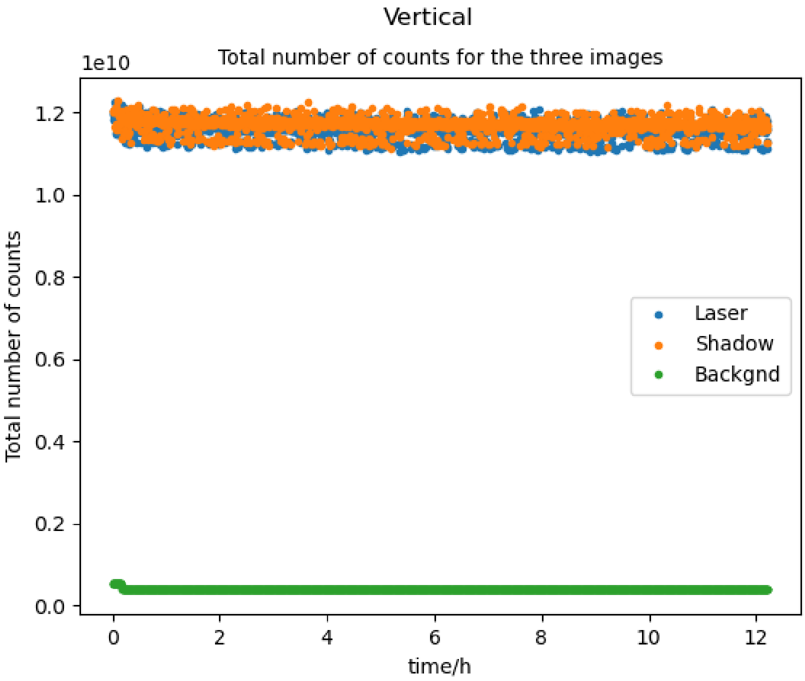

Figure 4.8: Noise measurement for long-time stabilisation. All counts are summarised for each image. The blue dots are the summarised pixels of the laser images, the orange for the shadow images and the green for the background images. Between each sequence, there was a 20 s break. The measurement was taken for 12 hours. The stabilisation over large time scales is sufficient.

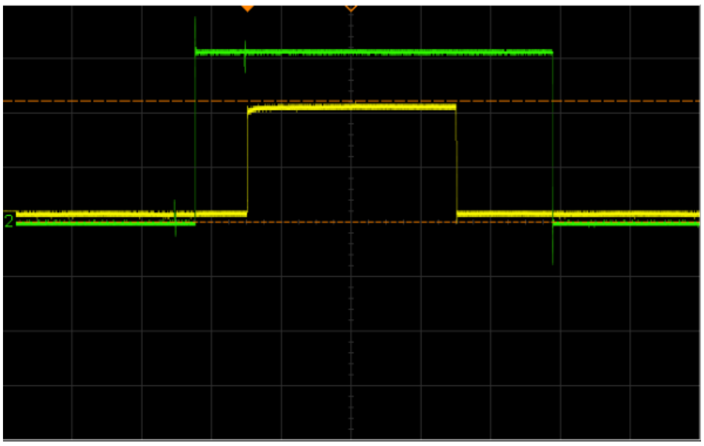

Figure 4.9: Overlap of the light on-time, measured with a photodiode (yellow) and the exposure duration time read from the camera (green).
V/DIV: 50 mV (AOM), 1 V (Camera); time/DIV: 20 μs

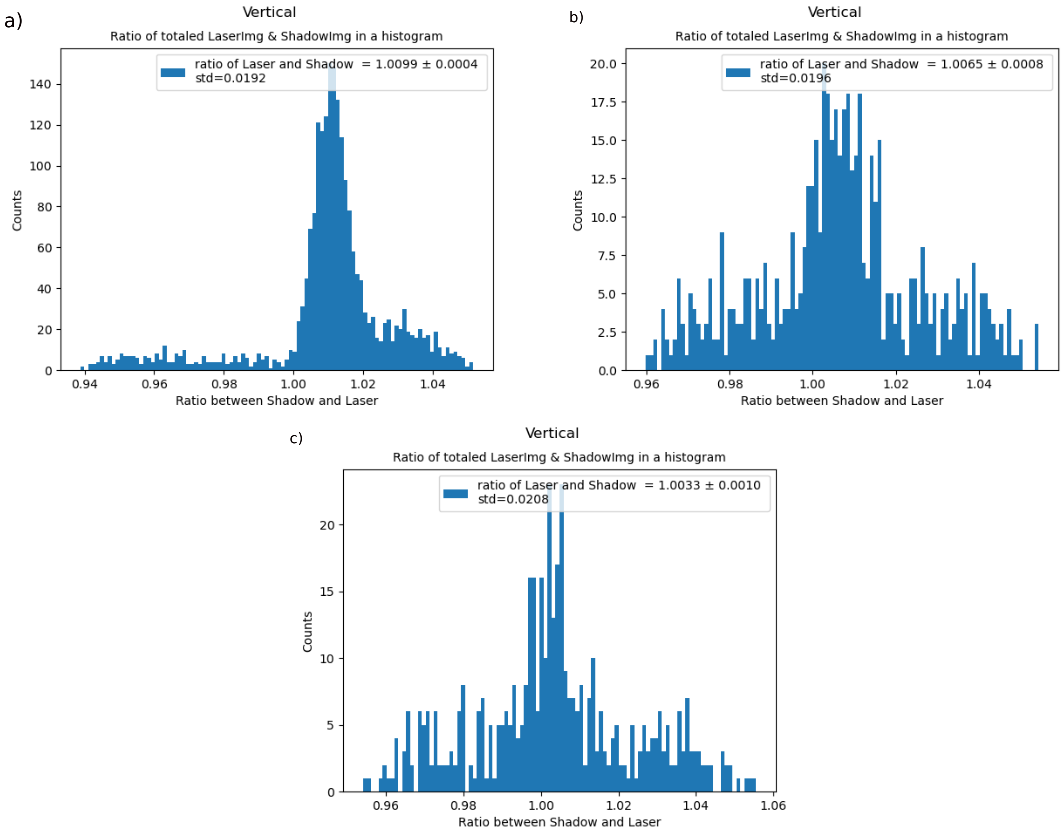

Figure 4.10: The ratio of the Laser and Shadow image. Left with a time between laser, shadow and background images of 70 ms, in the middle of 100 ms and right of 400 ms.

Another important point to consider is the uncertainty in the atom number caused by noise only. In general the atom number N_{atom} is calculated with equation 4.1. For the images without atoms inside the SC equation 4.1 gives an atom number of -10^5 with a time between images of 100 ms. The result of this measurement is shown in 4.11.

The minus sign is given due to the fact, that the counts in the shadow image are often higher compared to the counts in the laser image. Expected is the other way around because with the shadow image the absorption of the atomic cloud is detected and in the laser image the laser without the atomic cloud can be seen. The measured behaviour can be explained with a heating effect in the AOM during the sequence, which was investigated in figure 4.10.

Therefore the limit of the atom number that can be measured is 10^5. Since 10^9 atoms can be trapped in the MOT chamber, an atom number in the range of 10^7 is expected inside the SC. This is confirmed by a test measurement, see section 4.2.3.

In summary, the vertical imaging can be used to determine the atom numbers in the science chamber.

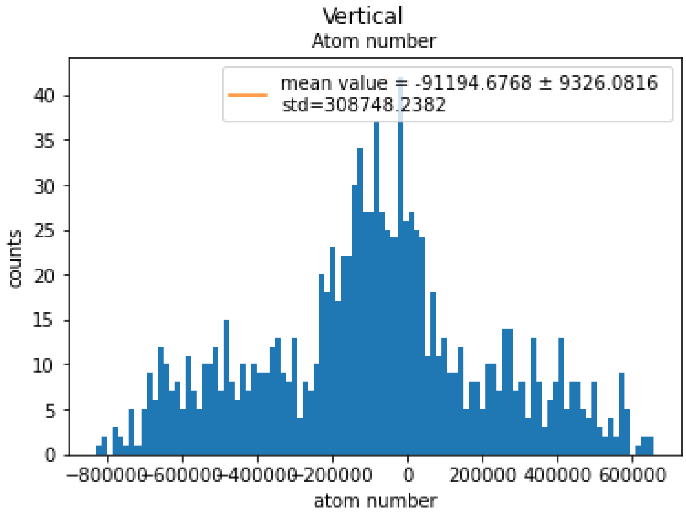

Figure 4.11: Apparent atom number which is calculated only from noise measurement.

4.2 Magnetic Transport

In this chapter, the magnetic transport is explained in detail. A schematic setup of the magnetic transport is shown in figure 4.12. First of all, the reason why a magnetic transport is used in this experiment is given. Afterwards, the working principle of the magnetic transport and the design are described. In section 4.2.2 the setup and the construction is shown. The magnetic transport sequence to get atoms into the SC is explained in section 4.2.3.

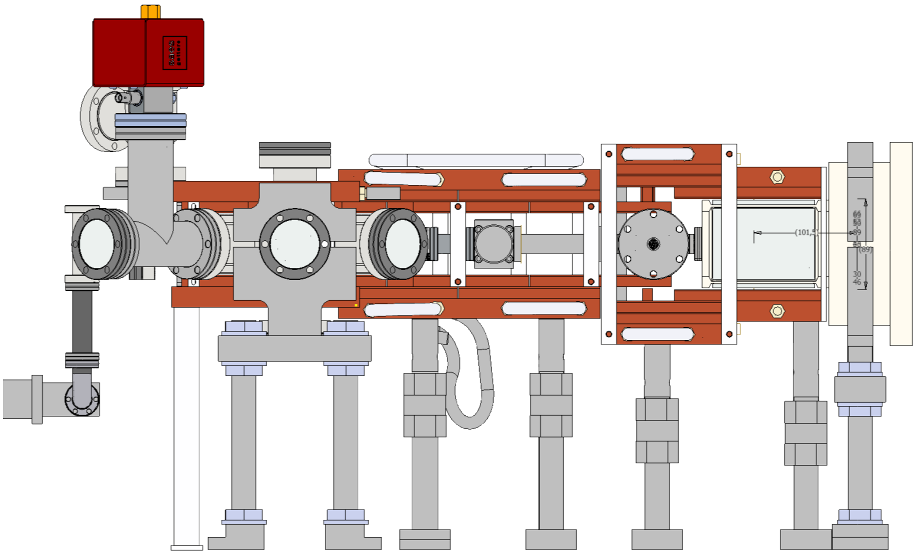

Figure 4.12: CAD sketch of the magnetic transport setup. The MOT chamber is located on the left-hand side and the science chamber on the right-hand side.

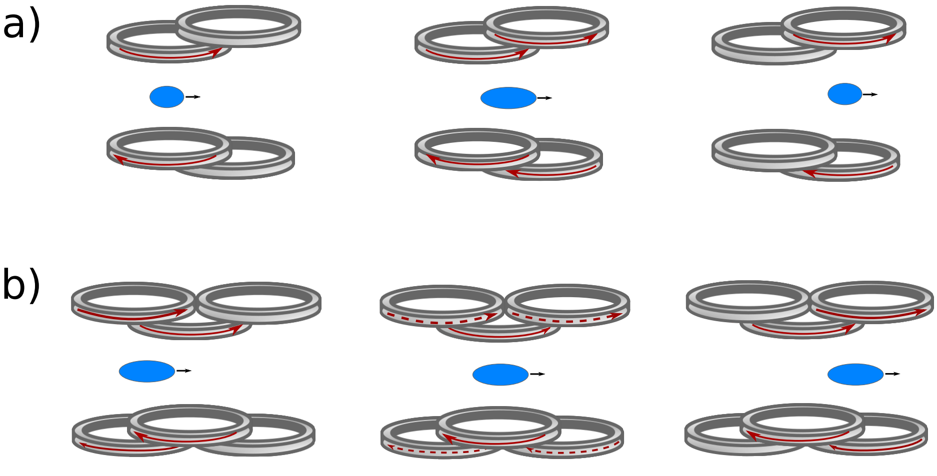

Figure 4.13: Sketch of the working principle of a magnetic transport.

4.2.1 Working Principle and Design

This section describes the design and working principle of the magnetic transport.
The cold atoms are prepared in the MOT chamber and then transported to the SC, see chapter 2. To transport the atoms different options are available. One option would be to transport the atoms with optical tweezers. Given the current design of the experiment, there is no space to integrate an optical transport. In addition, the scattered light in the environment would cause the system to heat up, which would counteract the cooling of the cryostat. To summarise, an optical transport is not a feasible option for this experiment.
A magnetic transport can be realised with a moving magnetic quadrupole coil or chain of stacked coils. The employed technique in this experiment is the latter to not have moving parts at the experiment. The atoms will be pumped into a low-field seeking state and so the atoms are trapped at the minimum of the quadrupole field.
In the following the design and the working principle of the magnetic transport in this experiment are explained.
The design of the magnetic coil assembly is inspired by the magnetic coil assembly design in reference [21]. The series of the magnetic coils can be separated into different magnetic coil pairs which are operated in the Anti-Helmholtz configuration. Due to the Anti-Helmholtz configuration, a quadruple potential is achieved. In the first coil pair, the atoms are trapped in the potential by running a suitable current through the coil pair. A second coil pair overlaps partly with the first coil pair, see figure 4.13. If the current in the first pair of coils is reduced and the current in the second pair of coils is increased at the same time, the quadrupole field moves continuously from the first to the second pair. As shown in figure 4.13, the trap expands along the transport direction between the two coils and then contracts back to a normal quadrupole when the position of the second pair of coils is reached. The use of a chain of several coil pairs increases the transport distance, but the repeated expansion and contraction leads to a heating of the atoms. By adding a third coil, which makes it possible to always run current through two coils, the expanded state of the trap is maintained until the last pair of coils is reached, see figure 4.13. For further details see in reference [21].

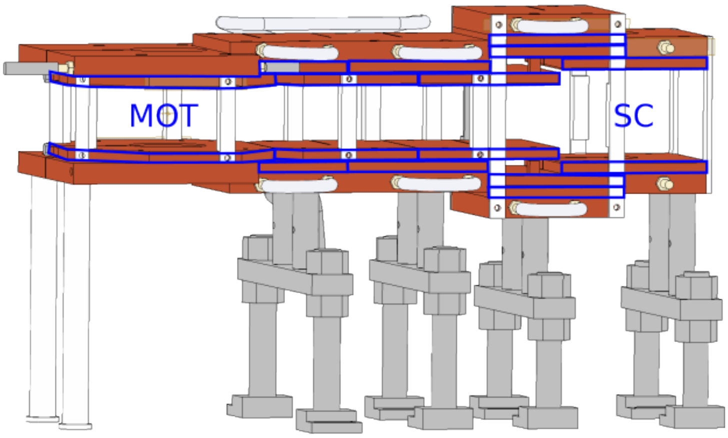

Figure 4.14: The magnetic transport assembly. The magnetic coils are indicated by blue boxes. On top or below the magnetic coils cooling blocks to cool the coils are placed. On the left side, the MOT chamber is placed and on the right side the science chamber.

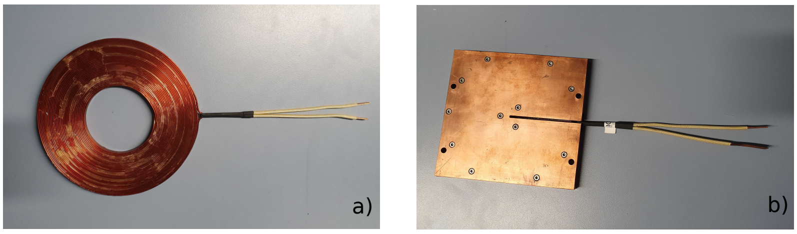

Figure 4.15: a) shows a coil before being glued inside a coil mount, b) shows a coil glued inside a coil mount. The coil mount has a slice to reduce Eddy currents.

In this experiment the atoms are transported over a distance of 450 mm with the described method. 16 coils are used which are mounted in seven different coil pairs, one is a double stack coil pair. It was decided that the maximum operating current of the transport should be 100 A and that the axial gradient during transport should be 130 $\mathrm{G\,cm^{-1}}$. This design choice, together with the constraints on the minimum distance of the coils from the transport axis given by the dimensions of the vacuum chamber, made it necessary to use a stack of two coil pairs at the second to last coil position in the transport chain. A schematic sketch of the assembly of the magnetic transport is shown in figure 4.14. The coils are placed in copper mounts. A photograph of a coil and a coil mount are shown in figure 4.15. The coil mounts have a slice to reduce Eddy currents.

4.2.2 Setup and Alignment

This section describes the assembly of the magnetic transport as well as the alignment.
As mentioned in 4.2.1 a maximal current of 100 A runs through the coils, and this high current causes some heating effects. To balance these heating effects cooling blocks are placed on the coil mounts. Water cooled to 17 °C flows in the cooling blocks.
Between the cooling blocks and the coil mounts is a thermal paste[11] to improve the thermal conductivity

---

[11] Keratherm-Wärmeleitpaste KP12 from Kerafol [88]

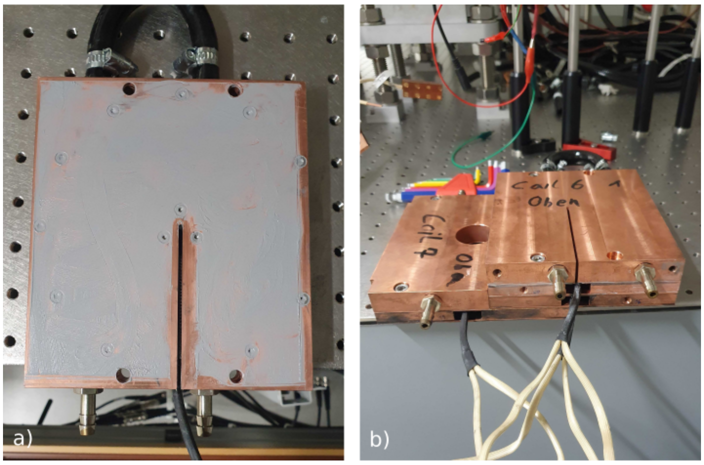

Figure 4.16: An example of the assembly of the coil mount and cooling block. In a), the thermal paste is applied to a coil mount. In b), the cooling block is placed on the coil mount, with the thermal paste between the two parts for better thermal conductivity. Water hoses are on the cooling blocks through which the cooled water flows.

between these two parts, see figure 4.16a). The overlapping coil mounts and cooling blocks are screwed together resulting in a rigid coil chain, see figure 4.16b).
The entire magnetic transport assembly can be seen in figure 4.17. The cooling blocks are supplied with cooled water via black plastic water hoses. Each coil is connected to power cables and has a temperature sensor screwed into its mount to monitor its temperature during operation.

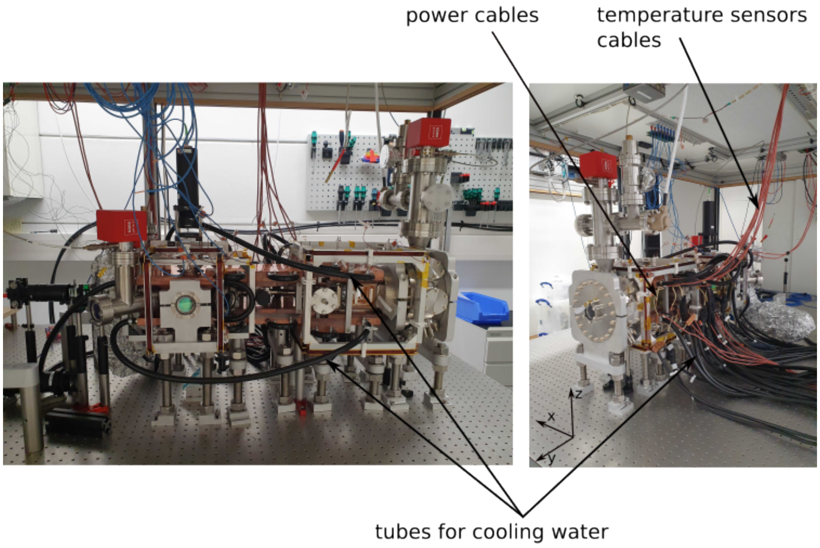

Figure 4.17: The entire magnetic transport assembly imaged from different angles. The tubes for cooled water, the temperature sensors and the cables to supply the coils with power are marked. In the right image also a coordinate system is shown.

Figure 4.18: The alignment of the SC. In a) the laser which represented the probe-control-setup is shown. With this laser, the SC is aligned. The back reflections on the edge of a paper are shown in b). The position alignment is shown in c) and d) for the z-axis position and the y-axis position, respectively.

Alignment of Vacuum System and Magnetic Transport

The MOT chamber, the science chamber and the magnetic transport coils must be properly positioned and aligned with each other. The desired final position of the atom cloud in the science chamber was fixed relative to the optical table. Since the inner assembly is rigidly connected to the science chamber, it was important to position the science chamber as precise as possible with respect to the desired final trap position.
To align the SC a laser which represented the probe-control-setup is set up on the breadboards, see figure 4.18a). The laser is aligned along the x-axis with two iris. The tilt angle of the science chamber was corrected by looking at the back reflection of the representative laser, see figure 4.18b). This was done for all three spatial axes. The position of the SC was set by using a paper sheet which has a length of 60 cm and 35 cm, which is equal to the position of the experimental plane in the SC. Therefore when the laser hits the end of the paper sheets the SC should be in the right position, see figure 4.18c) and d). This method has an uncertainty of around 1 mm, because of an uncertainty of 0.5 mm by cutting the paper sheets and afterwards an uncertainty of around 0.5 mm placing the paper sheets on the window.

For the successful transport of atoms it is especially crucial that the differential pumping tube is correctly aligned to the magnetic transport axis. The differential pumping tube is placed behind the

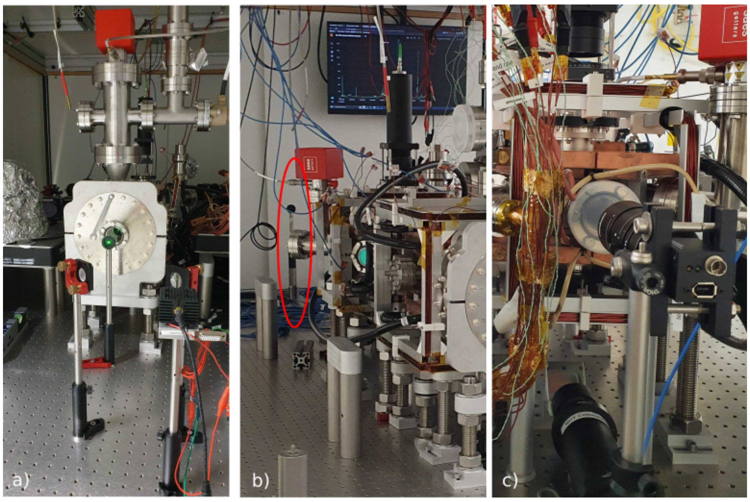

Figure 4.19: Construction for the alignment of the both chambers to each other. In a) the laser and the iris in front of the experimental setup and in b) the second iris behind the experimental setup are shown. The camera for imaging of the alignment beam is shown in c).

MOT chamber and differentiates the two different pressures in the two chambers, see section 2.1.1. For this alignment, a laser was directed along the y-axis, the magnetic transport axis, with one iris positioned in front of the experimental setup, which means in front of the octagon to which a viewport is attached, and another behind it, see figure 4.19a) and b). The laser beam is imaged with a camera mounted behind the MOT chamber, see figure 4.19c). When the beam is imaged on the camera a circle is expected when the beam goes perfectly through the experimental setup, but a caustic behaviour was observed, see figure 4.20a). This caustic was caused by the differential pumping tube, which is tilted relative to the y-axis. The position of the differential pumping tube is shown in figure 4.20b). The magnitude of this tilt was unexpected and was caused by a manufacturing error. The assumed reason for this is that the welding of the differential pumping tube to its flange has not been carried out perfectly, resulting in the tilting of the differential pumping tube. To compensate this angle, the differential pumping tube was tightened in such a way that the differential pumping tube was tilted in the other direction. In figure 4.20c) the flange of the differential pumping tube is coloured blue and the flange on which the differential tube can be tightened is coloured red, which means on the flange of the MOT chamber. To tighten the differential pumping tube with control different spacers were placed between these flanges and step by step the screws were tightened. While the screws were tightened, the alignment beam on the camera was observed to see if the clipping can be improved and the chamber pressure was monitored to ensure that no leak was introduced by the additional tightening. Figure 4.21 shows a laser beam imaged through the differential pumping tube a) before and b) after the angle alignment. Figure 4.21b) shows an improvement of the clipping of the beam but the beam is still clipped by the differential pumping tube. This is the final position of the differential pump tube as the physical limit has been reached as there is no room to tighten the flange of the differential tube any further.

After improving the alignment of the differential pumping tube as much as possible a first transport sequence was tested. The magnetic transport sequence and the result are described in the following section 4.2.3.

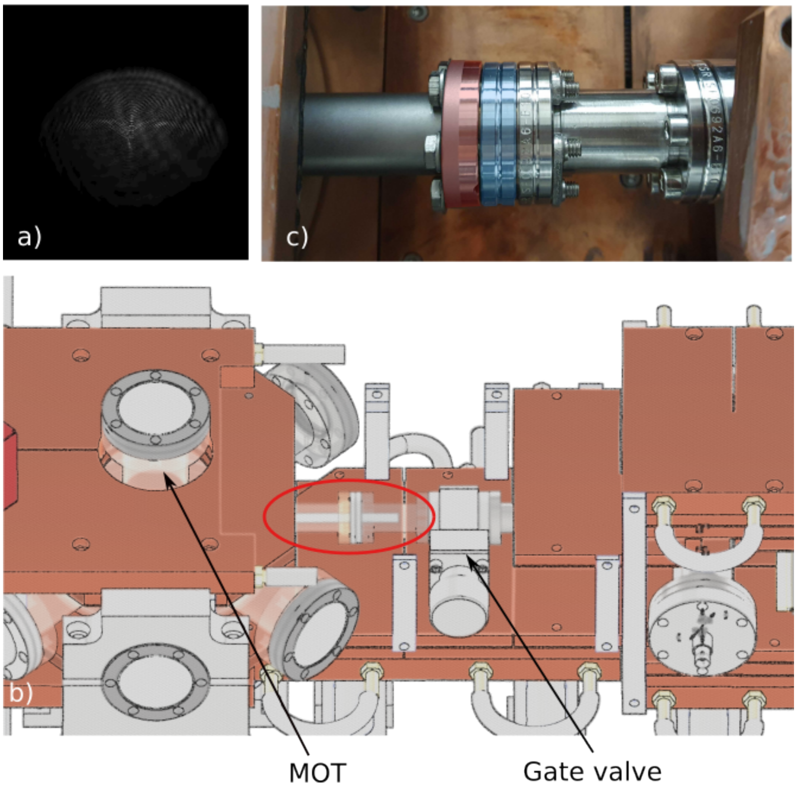

Figure 4.20: The alignment beam is reflected at the tilted differential pumping tube, which position is indicated in b) and c), and imaged on a camera, which is illustrated by the caustic behaviour on the camera, see a). In b) the differential pumping tube is marked with a red circle. The MOT chamber and the tube to the gate valve are transparent to show the geometry of the differential tube inside these tubes. In c), the flange of the differential pumping tube is coloured blue and the flange on which the differential pumping tube is tightened is coloured red.

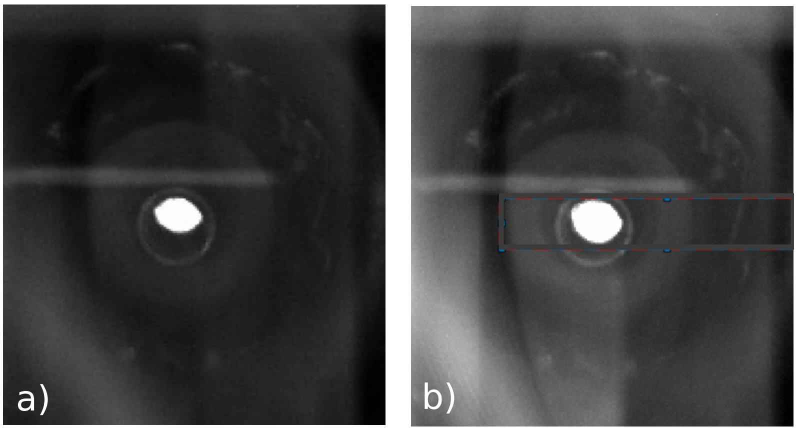

Figure 4.21: The imaged beam on the fluorescence camera after passing the differential pumping tube. In a) before and in b) after tilting the differential pumping tube.

4.2.3 Transporting Atoms into the Science Chamber

To transport the atoms from the MOT chamber to the science chamber the atoms have to be prepared in the MOT chamber beforehand. The different steps are: MOT loading (1), MOT compression (2), optical molasses (3), optical pumping (4) and magnetic transport (5). The MOT loading is briefly explained in the following, for more technical details see section 2.1.3. Steps 2,3 and 4 are only described theoretically because these steps were not done in this thesis. The procedure and optimisation of these steps can be read in the forthcoming master thesis of Julia Gamper.
During MOT loading, the atoms are trapped and cooled from the background gas for 1 s. The time-of-flight measurement technique can be used to determine the atom number and temperature after the MOT loading [89, 90]. By using this technique, the atom temperature of 400 μK and the number of atoms of 10^9 can be determined at a magnetic gradient of the MOT of 10.5 G cm^{-1}. Afterwards, the atomic cloud is compressed to achieve a smaller size of the atomic cloud. This cloud can then be transported to the SC without significant atom loss at the differential pumping tube. The compression is done by increasing the magnetic gradient of the MOT fast, which means $<$ 100 ms. In the next step, the optical molasses is generated by turning off the magnetic fields. The aim of the optical molasses is to reduce the temperature of the atoms without loss of atom density. This step should take about 10 ms and a final temperature of 50 μK is expected, see for example in reference [91]. During the writing of this thesis, an optical molasses with a temperature of 40 μK was achieved in the laboratory. After the optical molasses, the atoms are optically pumped to the $F = 2, m_F = 2$ state, since this state is a stable low-field-seeking state and can therefore be trapped in a magnetic quadrupole trap [33, 92]. With perfect optical pumping it is in principle possible to transfer all atoms in the cloud to the magnetic trap since all atoms will be in a low-field-seeking state. This step will take around 0.1 ms. After the optical pumping, the magnetic transport is started. The working principle of the used magnetic transport is explained in section 4.2.1.

In order to test whether atoms can be transported into the science chamber, only the MOT loading and magnetic transport steps were carried out. Steps 2-4 were not implemented during this thesis due to time constraints. Omitting these steps leads to a lower transfer efficiency from the MOT to the magnetic trap due to the lack of optical pumping and to a hotter atom cloud in the magnetic trap due to the lack of molasse cooling and compression before the transfer. Nevertheless, an atom number of $> 10^9$ atoms after loading the MOT is sufficient to test the transport, because even with the additional losses and the higher temperature, the absorption imaging in the science chamber, which can detect atom numbers of about $> 10^5$, is sensitive enough to detect the transported atoms. After the magnetic transport, three images for the absorption imaging were taken as explained in 4.1.1. The MOT loading, the magnetic transport and the three taken images of the absorption imaging form the sequence used for testing the atomic transport. This sequence is shown in figure 4.22. Each part required for this transport can be controlled by the experiment control software by applying analogue control voltages or digital signals. Each part has an assigned channel via which the software controls the respective part within the sequence.

With channel 1 (blue line), the power is controlled by the laser cooler, which means at what point in the sequence the MOT is loaded. Accordingly, in figure 4.22 is illustrated that this sequence begins with a MOT loading. Channel 2 to 5 show the voltage used to control the current through the seven coil pairs for the magnetic transport. Note that only four analogue channels are used for seven coil pairs. This is

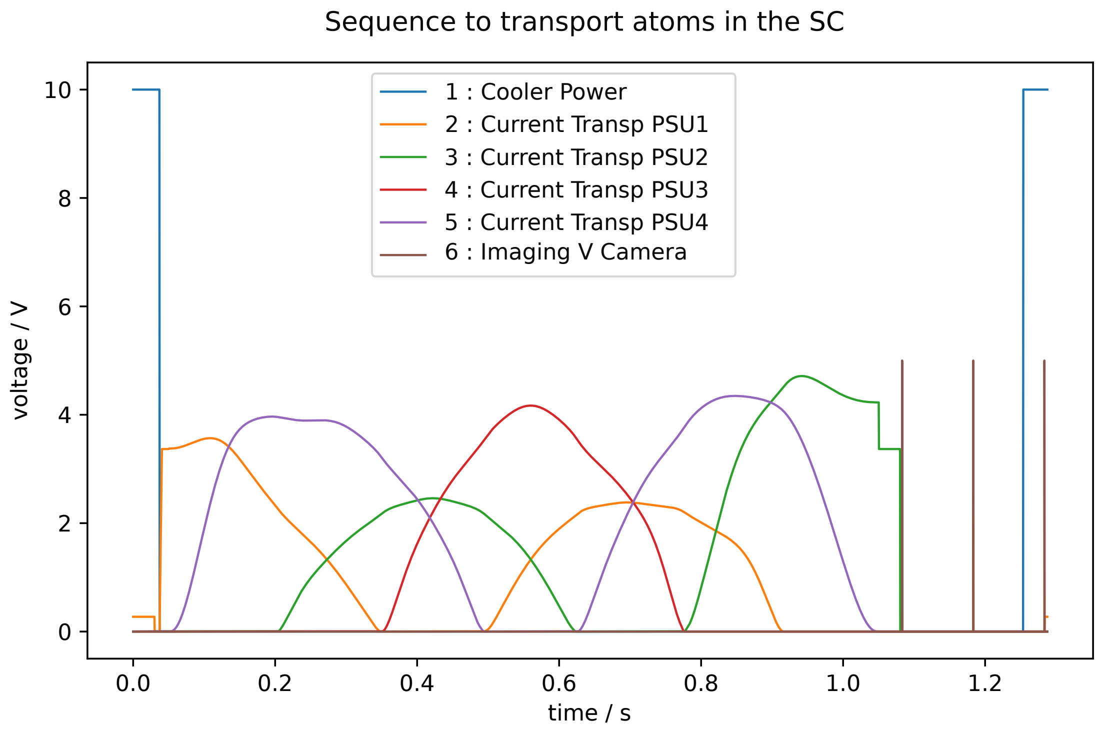

Figure 4.22: The entire magnetic transport sequence. The MOT is loaded for 1 s, indicated by the blue line. Then current runs through the seven magnetic coil pairs for 1.2 s. At the end, three images are taken for the absorption imaging, indicated by the brown line.

possible because some power supply units (PSU) are used for two coil pairs in a sequence at different times. The three brown lines at the end indicate the three images required for the absorption imaging. This sequence can be used to image an optical density distribution in the SC with the absorption imaging. The resulting measurement is shown in figure 4.23. Using the formula 4.1, it is determined that 10^7 atoms are transported from the MOT chamber to the science chamber, which means over a distance of 450 mm.

In summary, it is possible to transport 10^7 atoms into the science chamber with this assembly and alignment. This measurement was done without optimisation of the MOT loading and the magnetic transport and without the steps of the optical pumping, optical molasses and MOT compression. Including these steps and optimising the transport sequence a higher number of transported atoms is expected.

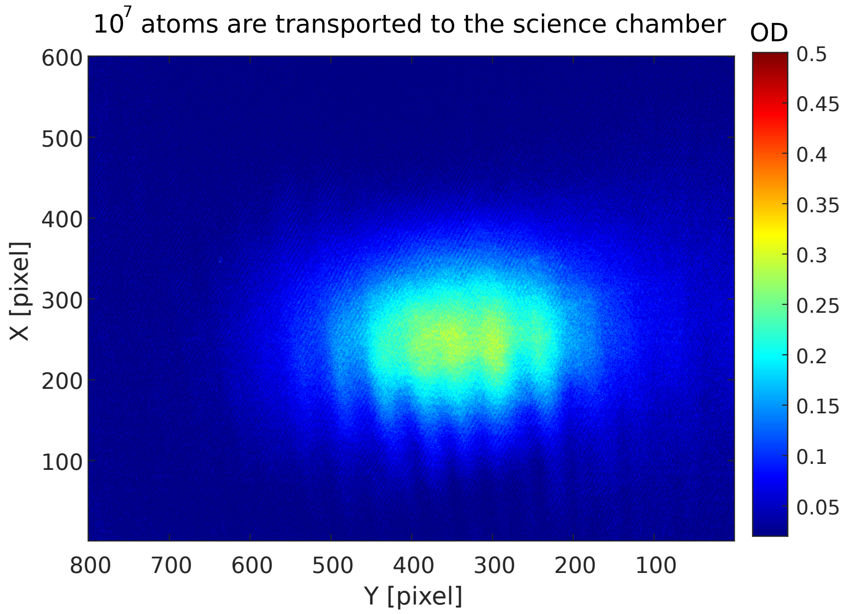

Figure 4.23: The imaged optical density distribution in the science chamber after 1 s MOT loading and a magnetic transport sequence. From the optical density distribution, an atom number of 10^7 is determined. The y-axis is the magnetic transport axis.

CHAPTER 5

Rydberg Excitation Probe Laser

In this experiment, different lasers are required for different experimental steps, for example, the Cooler laser and the Repumper laser for the cooling procedure, see chapter 2.1.2. These lasers are set up on a separate table, the so-called laser table. The light is transported to the experiment via fibres. The laser table is briefly explained in 5.1. Then, in section 5.2 the laser setup is explained, which is required for the vertical absorption imaging and the probe beam in the planned probe-control-setup for Rydberg excitation, which was set up as a part of this thesis.

5.1 Overview of the Laser Table

This section briefly describes the part of the laser table on which the used lasers in the current experiment are mounted. This part of the laser table is shown in figure 5.1.
Five lasers are set up on the laser table. Further lasers are built on the laser table but are not yet set up or in operation. For example, a 960 nm laser is set up on the table and stabilised with the cavity, but as this laser was not used in this work, it is not explained in the following [93]. One laser, the Cooler laser, uses a tapered amplifier laser system (TAPro). The other lasers are tunable diode lasers. All lasers are from Toptica. The different wavelengths of the five lasers are summarised in table 5.1.
The so-called master laser is installed in the orange-coloured box in figure 5.1. The frequency of the master laser is fixed to the frequency of an optical cavity, using the Pound-Drewer-Hall stabilisation method [94, 95]. The cavity is the silver cylinder mounted on the laser table in the top left-hand corner. The other four lasers, the slave lasers, are stabilised relative to the frequency of the master laser via

Laser	Transition	Wavelength
Master	$^{85}\mathrm{Rb}(3 \longrightarrow 3,4)$	780.2438 nm [32]
Cooler	$^{87}\mathrm{Rb}(2 \longrightarrow 3)$	780.2461 nm [33]
Repumper	$^{87}\mathrm{Rb}(1 \longrightarrow 2)$	780.2327 nm [33]
DLPro4	$^{87}\mathrm{Rb}(2 \longrightarrow 2)$	780.2466 nm [33]
DLPro3	$^{87}\mathrm{Rb}(2 \longrightarrow 3)$	780.2461 nm [33]

Table 5.1: The transition and wavelength for the five different lasers

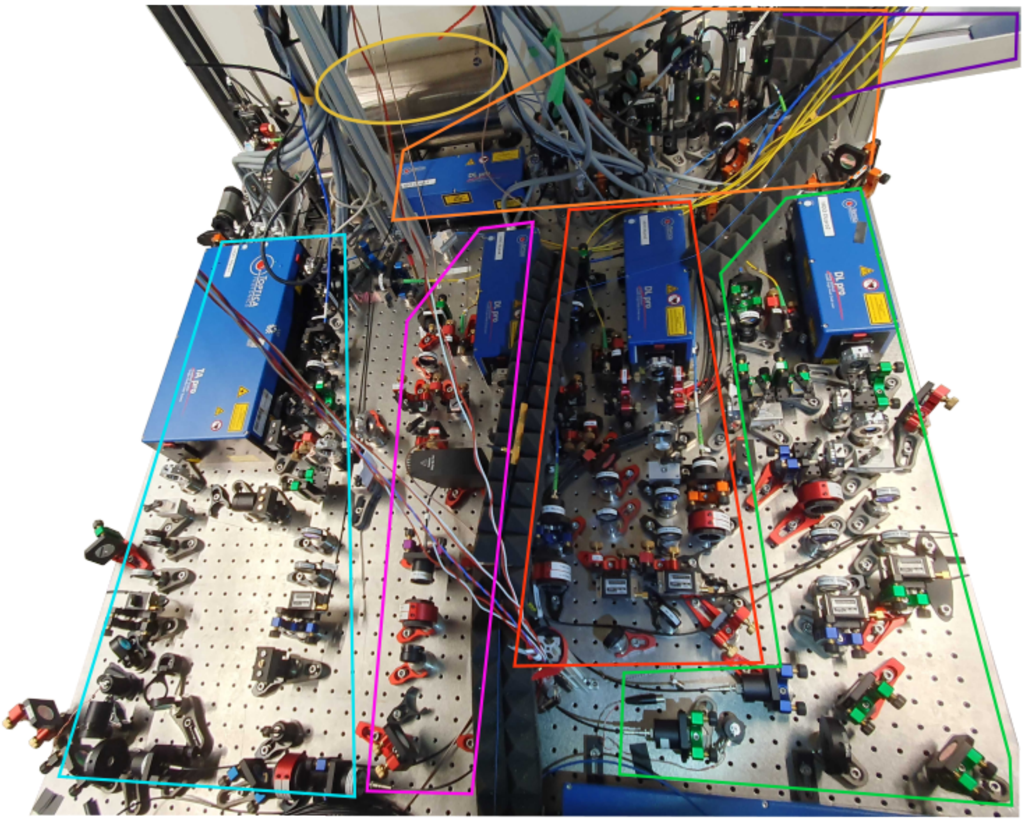

Figure 5.1: An overview of the laser table. There are currently five lasers on the laser table set up, which are currently used in the experiment and each laser setup is marked with a coloured box. The master laser is in the orange-coloured box and the other lasers are set to the wavelength of the master laser. The master laser is locked to a frequency of a cavity, which is the silver cylinder in the top left-hand corner, marked by the yellow circle. In the light-blue-coloured box, the Cooler laser is set up and in the green-coloured box the Repumper laser. The DLPro4 is set up in the purple-coloured box. In the red-coloured box, the DLPro3 is set as part of this thesis.

beat note locks[94][95].
The slave lasers are coupled to fibres that are guided from the laser table to the experiment table via a fibre bridge, as indicated by the dark purple box in the top right-hand corner of the figure 5.1.
In the turquoise-coloured box, the Cooler laser is set up. One arm is used for the cooling procedure for the magneto-optical trap (MOT), see chapter 2.1.2. The other arm is used for the absorption imaging at the MOT chamber. The Repumper laser is set up in the green-coloured box. This setup has two different arms, as well. One arm is used for the repumper beam in the cooling procedure for the MOT and the other arm is used as the repumper beam, which is required for optical pumping. The arms of the Cooler and the Repumper, which are used for the MOT are intensity-locked.
In the purple-coloured box the DLPro4 laser can be seen. The DLPro4 laser is used for the optical pumping. The DLPro3 is set up in the red-coloured box and also with two different arms. One arm is used for the absorption imaging at the science chamber. The other arm will be used for the probe beam for the planned probe-control-setup. In the current experiment, this arm is used for the horizontal absorption imaging at the science chamber. This laser was set up during this thesis and the setup will

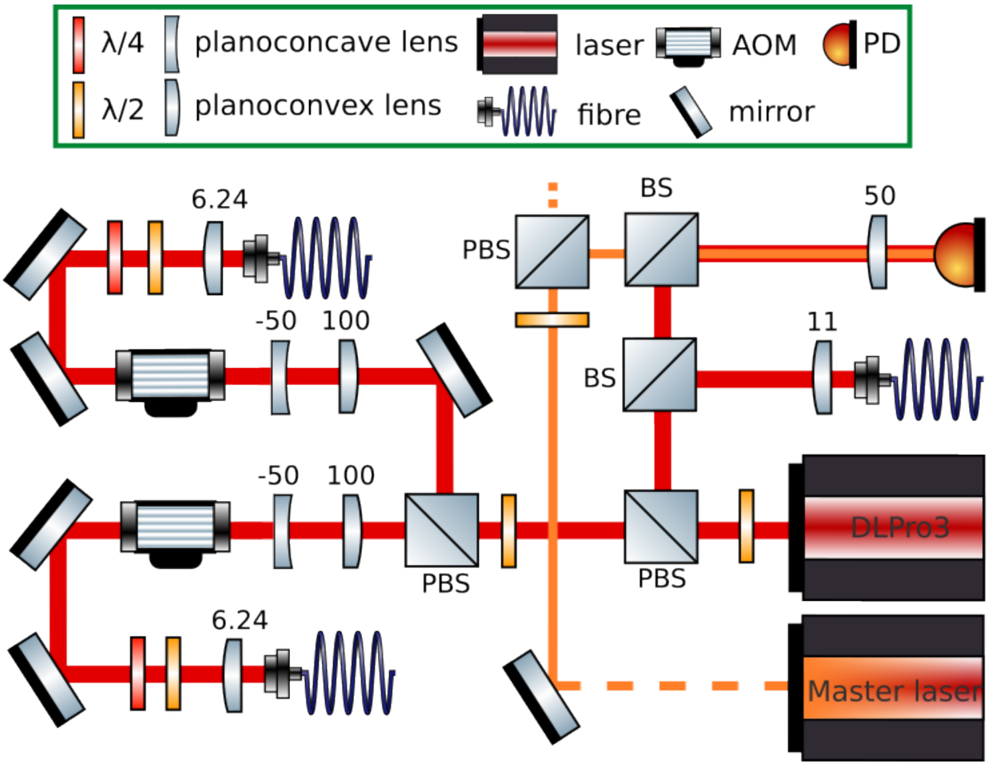

Figure 5.2: The entire setup of the DLPro3 laser, which is used for the vertical absorption imaging at the science chamber and for the probe beam for the planned probe-control-setup. The numbers over the lenses state the different focus lengths in units of mm. The arm of the transmitted beam behind the second PBS is used for the absorption imaging and the reflected beam for the probe beam. For the beat note lock, the master laser (indicated by an orange line for better differentiation) and the DLPro3 laser (indicated by a red line) are overlapped on a photodiode (PD).

be explained in more detail in the following section 5.2. This laser setup is representative for the other laser setups.

5.2 Setup

This section describes the laser setup for the probe beam and the vertical absorption imaging beam for the science chamber. The setup is shown in figure 5.2. The setup can be divided into two parts. One is required for the beat note lock and the other part is required to couple the beam into two different fibres. The first PBS behind the DLPro3 splits the beam into both parts. First, the part that is required for the beat note lock is explained. Then the part for the coupling into the two fibres to guide the beams to the experiment will be discussed.
The laser in this setup is a tunable diode laser from Toptica (DLPro). The frequency of this laser is stabilised to the master frequency via a beat note lock. The master laser is also set up on the table, see figure 5.1. The master beam passes several optical parts until the beam reaches the DLPro3 setup. Therefore, the master beam is dashed up to the mirror to indicate this. The transition of the DLPro3 laser is $^{87}\mathrm{Rb}(F = 2 \rightarrow F' = 3)$ and of the master laser $\mathrm{Rb}^{85}(F = 3 \rightarrow F' = 3, F' = 4)$. Therefore

Laser arm	AOM			Fibre		
	Power in front	Power behind	CE	Power in front	Power behind	CE
Imaging	80.4 mW	65.2 mW	81.1%	64.4 mW	40.0 mW	62.1%
Probe	4.0 mW	3.6 mW	90%	3.5 mW	2.5 mW	71.4%

Table 5.2: Coupling efficiency (CE) of Imaging arm and Probe arm of the AOM and the fibre.

the beat note is at -1.066 MHz. The 80 MHz frequency shift of the acousto-optic modulator (AOM) must also be taken into account, which results in a beat note of -1.146 MHz. The beat note lock is done in the setup as follows.
With the $\lambda/2$ waveplate behind the DLPro3 laser, the power of the beam can be adjusted behind the PBS. The beam is then reflected off a polarising beamsplitter (PBS) and then transmitted through a beamsplitter (BS) and then reflected at a second BS. The DLPro3 beam is then focused onto a photodiode (PD) using a planoconvex lens with $f = 50$ mm. The power of the master beam is adjusted with a $\lambda/2$ waveplate in front of a PBS on which the master beam is transmitted to the DLPro4 and then to the Cooler setup, which is indicated with a dashed line in figure 5.2. The laser beam from the master laser and the beam from DLPro3 are overlapped on a PBS and focused on the PD with the convex lens. With the two $\lambda/2$ waveplates, both beams are set to the same power of 1 mW.
The DLPro3 beam is also reflected by the first BS. The reflected beam is focused on a fibre to a wavemeter using a planoconvex lens with $f = 11$ mm. With the wavemeter, the wavelength can be monitored.
With this described setup the required wavelength for the experiment can be checked and stabilised with the beat note lock.

The DLPro3 beam is reflected off the first PBS into the setup described above and transmitted into the part of the setup described below. This part of the setup is used to couple the laser into two different fibres.
The transmitted beam passes a combination of a $\lambda/2$ waveplate and a PBS to achieve a splitted laser beam with a controlled power ratio. This PBS splits the beam into the two different arms for the coupling into the two fibres. The setups of the two arms are the same, so only one arm is explained. Behind the PBS, the beam passes through a Galilean telescope setup with a planoconvex lens with $f = 100$ mm and a planoconcave lens with $f = -50$ mm, resulting in a magnification factor of 0.5. This telescope is used to reduce the beam diameter and thus, reduce clipping effects as the beam enters the AOM. The AOM is adjusted so that the beam is refracted to the first order with a high efficiency. The coupling efficiency in the first order of both arms is given in table 5.2. The beam is then reflected by two mirrors onto two waveplates. One $\lambda/4$ and one $\lambda/2$ waveplate. With this configuration, all values of beam polarisation can be achieved on the Poincaré sphere. The first order of the beam is then focused using a planoconvex lens with $f = 6.24$ mm in a fibre. The coupling efficiency into the fibre is given in table 5.2 for both arms. Due to the AOM and the first order coupling in front of the fibre, the beam can be switched off during the experiment and switched on again if required, which gives precise control over the measurement and allows specific experimental sequences.

CHAPTER 6

Conclusion and Outlook

In this thesis, I was part of upgrading an experimental setup for trapping and cooling of rubidium. The goal of the setup is to integrate rubidium Rydberg atoms with an electro-mechanical oscillator for hybrid quantum optics. At the start of this thesis, the experimental setup consisted of ^{87}Rb atoms in a commercial vacuum chamber. During this thesis, an ultra-high vacuum chamber was designed and built to allow connection to a 4 K cryostat. To transport atoms from the MOT region into this new vacuum chamber that in the future will host the cryostat shields, a magnetic transport was set up to transport atoms from the MOT chamber into the new chamber.
Since the cryostat will be delivered in summer 2024, this thesis was done with the setup at room temperature.

The ultra-high vacuum chamber was built during this thesis is a homemade glass cell with a frame of titanium. The cell windows are glued to the frame with two-component vacuum-compatible epoxy glue. During this thesis, a successful glueing method was developed for connecting NBK-7 glass to the titanium frame. This involved improving the adhesion between the titanium, the NBK-7 glass and the epoxy glue. The birefringence of the windows was investigated by measuring the polarisation extinction ratio (PER) after the glueing process. A low PER is important for the optical experiments in the science chamber. For example for addressing specific atomic transitions in the hyperfine basis and driving closed optical transitions. For a defined position of the window through which the axis of the laser beam passes, the low PER value is particularly important. The measured PER value of 10^{-5} is more than sufficient for the requirement in this experiment. Apart from having a low birefringence, the cell must also be vacuum-tight. Before baking the cell was pumped down to 10^{-7} mbar after 20 h pumping time, and the cell developed no leaks after a stress test by baking the cell. The cell was installed in the experimental setup and connected to an ion and a NEG pump and a vacuum of 10^{-10} mbar was achieved.
The experiment will be used for working with Rydberg atoms, which are very sensitive to and can be ionised with electric fields. An assembly for generating the ionisation electric field close to the cold atoms was mounted inside the vacuum chamber. When the atoms are ionised, the ions are then detected via a multi-channel-plate. The ion detection was set up during this thesis. Since Rydberg excitations cannot be made in the experiment yet, the ion detection setup was not tested with ions.
At the start of this thesis a chamber to load atoms with a magneto-optical trap and prepare the atoms was already built and aligned. This chamber has a high rubidium background pressure to allow a

fast atom loading. A lower vacuum pressure is required in the science chamber for later Rydberg experiments. Therefore, the homemade science chamber is connected via a differential pumping tube to the loading chamber. The prepared cold atoms are transported from the loading chamber to the science chamber via magnetic transport. After assembly and alignment of the magnetic transport and installing the homemade vacuum cell, the magnetic transport into this chamber was tested. This sequence consists of an MOT loading of 1 s, a magnetic transport sequence and then taking three images for the absorption image. With this sequence and without further optimisation 10^7 atoms can be transported into the science chamber.

To detect if atoms can be transported into the science chamber an absorption imaging system was built at the science chamber. The imaging setup was built for the horizontal axis as well as for the vertical axis. With these two imaging setups, the position of the atoms can be detected in three dimensions and so the magnetic transport can be aligned.

For the imaging a 780 nm laser was set up. The laser was frequency stabilised via beat note lock to a so-called master laser, which is frequency stabilised to a resonator with the Pound-Drewer-Hall stabilisation method. The output of the imaging laser was split into two arms, one for each imaging direction. In each arm, an acousto-optic modulator was built in to control the two laser beams separately. These two laser beams are fibre-coupled to guide the light to the experimental setup. At the moment both arms are used for the absorption imaging at the science chamber. In the later stage of this experiment, one arm will be used for the probe beam by the Rydberg excitation.

The next step in the experiment will be to optimise the atom number and the temperature of the final atomic cloud in the science chamber. For this, the MOT loading will be improved and the steps of optical pumping, optical molasses and compression of the MOT will be included. In addition, the magnetic transport sequence can be improved in terms of the temperature and number of the atoms in the science chamber. The improvement can be realised by changing the velocity and the acceleration of the atoms during the magnetic transport. This involves a well-controlled turning on and off of the different coil pairs along the path.

In addition, the probe-control setup will be built at the science chamber and the transported atoms can be excited to Rydberg states with a well-defined polarisation. The test of ion detection can then be performed at room temperature.

In summer 2024 the cryostat will be delivered and attached on the science chamber. Following this Rydberg atoms can be excited and detected in a cryogenic environment. An even further step for the experiment is the inclusion of the atom-chip for hybrid quantum optics.

Bibliography

[1] N. J. Lambert, A. Rueda, F. Sedlmeir and H. G. L. Schwefel, *Coherent Conversion Between Microwave and Optical Photons—An Overview of Physical Implementations*, Advanced Quantum Technologies **3** (2020) 1900077.

[2] N. Lauk et al., *Perspectives on quantum transduction*, Quantum Science and Technology **5** (2020) 020501.

[3] I. Mahboob and H. Yamaguchi, *Bit storage and bit flip operations in an electromechanical oscillator*, Nature Nanotechnology **3** (5 2008) 1748.

[4] Y. Chu et al., *Quantum acoustics with superconducting qubits*, Science **358** (2017) 199, ISSN: 1095-9203.

[5] X. Han, C.-L. Zou and H. X. Tang, *Multimode Strong Coupling in Superconducting Cavity Piezoelectromechanics*, Phys. Rev. Lett. **117** (12 2016) 123603.

[6] A. D. O'Connell et al., *Quantum ground state and single-phonon control of a mechanical resonator*, Nature **464** (7289 2010) 1476.

[7] F. Arute et al., *Quantum supremacy using a programmable superconducting processor*, Nature **574** (2019) 505.

[8] M. Bild et al., *Schrödinger cat states of a 16-microgram mechanical oscillator*, Science **380** (2023) 274.

[9] R. Stevenson, J. ř. Miná ř, S. Hofferberth and I. Lesanovsky, *Prospects of charged-oscillator quantum-state generation with Rydberg atoms*, Phys. Rev. A **94** (4 2016) 043813.

[10] Y. Chu and S. Gröblacher, *A perspective on hybrid quantum opto- and electromechanical systems*, Applied Physics Letters **117** (2020) 150503, ISSN: 0003-6951.

[11] J. D. Teufel et al., *Circuit cavity electromechanics in the strong-coupling regime*, Nature **471** (7337 2011) 204.

[12] J. D. Teufel et al., *Sideband cooling of micromechanical motion to the quantum ground state*, Nature **574** (2019) 505.

[13] A. P. Higginbotham et al., *Harnessing electro-optic correlations in an efficient mechanical converter*, Nature Physics **14** (2018) 1038, ISSN: 1745-2481.

[14] A. Bozkurt et al., *A quantum electromechanical interface for long-lived phonons*, Nature Physics **19** (9 2023).

[15] M. Mirhosseini, A. Sipahigil, M. - Kalaee and O. - Painter, *Superconducting qubit to optical photon transduction*, Nature **588** (7839 2020) 1476.

[16] R. Löw et al., *An experimental and theoretical guide to strongly interacting Rydberg gases*, Journal of Physics B-atomic Molecular and Optical Physics **45** (2012).

[17] M. Saffman, T. G. Walker and K. Mølmer, *Quantum information with Rydberg atoms*, Rev. Mod. Phys. **82** (3 2010) 2313.

[18] J. A. Sedlacek et al., *Microwave electrometry with Rydberg atoms in a vapour cell using bright atomic resonances*, Nature physics **8** (2012) 819.

[19] H. Han, *Effect of Phonon Interference on the Thermal Conductivity and Heat Carriers*, University Paris-Saclay, 2015.

[20] J. Fortágh and C. Zimmermann, *Magnetic microtraps for ultracold atoms*, Rev. Mod. Phys. **79** (1 2007) 235.

[21] M. Greiner, I. Bloch, T. W. Hänsch and T. Esslinger, *Magnetic transport of trapped cold atoms over a large distance*, Phys. Rev. A **63** (3 2001) 031401.

[22] K.-N. Schymik et al., *Single Atoms with 6000-Second Trapping Lifetimes in Optical-Tweezer Arrays at Cryogenic Temperatures*, Physical Review Applied **16** (2021).

[23] *Pfeiffer Vacuum, viewport DN 40 CF Data Sheet*, `https://www.pfeiffer-vacuum.com/productPdfs/420GSG040.en.pdf`, visited on 22.02.2024.

[24] P. V. GmbH, ed., *The Vacuum Technology Book Volume2*, 2015.

[25] *SAES, NEXTorr® Z 200*, `https://www.saesgetters.com/wp-content/uploads/sites/5/2024/02/NEXTorr_Z_200_2024.pdf`, visited on 22.02.2024.

[26] *Thermo Fisher Scientific Chemicals, Rubidium 99.75*, `https://www.thermofisher.com/order/catalog/product/010315.06?SID=srch-srp-010315.22`, visited on 22.02.2024.

[27] *Pfeiffer Vacuum, DN16CF manual UHV gate valve*, `https://www.pfeiffer-vacuum.com/en/products/valves-chambers-components/vacuum-valves/isolation-valves/uhv-gate-valves/42368/uhv-gate-valve-dn-16-cf-metric-manual-ss-cu-fkm`, visited on 22.02.2024.

[28] I. I. Ryabtsev, I. I. Beterov, D. B. Tret'yakov, V. M. Èntin and E. A. Yakshina, *Spectroscopy of cold rubidium Rydberg atoms for applications in quantum information*, Physics-Uspekhi **59** (2016) 196, ISSN: 1468-4780.

[29] J. Wang, J. Bai, J. He and J. Wang, *Single-photon cesium Rydberg excitation spectroscopy using 318.6-nm UV laser and room-temperature vapor cell*, Opt. Express **25** (2017) 22510.

[30] J. T. Wilson et al., *Trapping Alkaline Earth Rydberg Atoms Optical Tweezer Arrays*, Phys. Rev. Lett. **128** (3 2022) 033201.

[31] D. R. L. (Ed.), ed., *CRC Handbook of Chemistry and Physics*, 81st edition, Boca Raton: CRC Press, 2000 728, ISBN: ISBN 0-8493-0481-4.

[32] *Daniel A. Steck, Rubidium 85 D Line Data (revision 2.3.2,10 September 2023)*, `https://steck.us/alkalidata/rubidium85numbers.pdf`, visited on 22.02.2024.

[33] *Daniel A. Steck, Rubidium 87 D Line Data (revision 1.6, 14 October 2003)*, `https://steck.us/alkalidata/rubidium87numbers.1.6.pdf`, visited on 22.02.2024.

[34] M. Egorov et al., *Measurement of s-wave scattering lengths in a two-component Bose-Einstein condensate*, Phys. Rev. A **87** (5 2013) 053614.

[35] S. L. Cornish, N. R. Claussen, J. L. Roberts, E. A. Cornell and C. E. Wieman, *Stable* ^{85}Rb *Bose-Einstein Condensates with Widely Tunable Interactions*, Phys. Rev. Lett. **85** (9 2000) 1795.

[36] *Accu-Glass Products, Glass metal transistion (Pyrex and stainless steel)*, `https://www.accuglassproducts.com/glass-tube-adapters/non-magnetic-adapters/open-single-flange/open-cf/075-133-non-magnetic`, visited on 31.03.2024.

[37] T. Gallagher, ed., *Rydberg atoms*, Cambridge University Press, 1994.

[38] K. C. Smyth, J. A. Schiavone and R. S. Freund, *Dissociative excitation of N2 by electron impact: Translational spectroscopy of long-lived high-Rydberg fragment atoms*, The Journal of Chemical Physics **59** (1973) 5225, ISSN: 0021-9606.

[39] F. J. Deck, E. A. Hessels and S. R. Lundeen, *Population of high-L sulfur Rydberg levels by ion–Rydberg-atom charge exchange*, Phys. Rev. A **48** (6 1993) 4400.

[40] N. Stiesdal, *Collective atom-light interactions with Rydberg superatoms*, University of southern denmark, 2022.

[41] E. Brion, L. H. Pedersen and K. Mølmer, *Adiabatic elimination in a lambda system*, Journal of Physics A: Mathematical and Theoretical **40** (2007) 1033, ISSN: 1751-8121.

[42] *Kimball Physics Spherical, octagon vacuum chamber*, `https://www.kimballphysics.com/product/mcf800-sphoct-g2c8/`, visited on 09.03.2024.

[43] *SAES, NEXTorr® D 500-5*, `https://www.saesgetters.com/wp-content/uploads/sites/5/2024/02/NEXTorr_D500_5_2024-1.pdf`, visited on 09.03.2024.

[44] *Allectra, SHV CF40 feedthrough*, `https://shop.allectra.com/products/241-shv-c40-4`, visited on 09.03.2024.

[45] *Infleqtion, atomic prisms, UHV glass cells*, https://www.infleqtion.com/atomic-prisms, visited on 20.02.2024.

[46] W. Demtröder, ed., *Experimentalphysik 2: Elekrizität und Optik*, 7th edition, Springer, 2018, ISBN: ISBN 978-3-662-55789-1.

[47] *Allectra, High vacuum leak sealant (Vacseal)*, https://shop.allectra.com/products/330-vacseal-s, visited on 24.03.2024.

[48] *EPO-TEK H77S - Technical Data Sheet*, https://www.epotek.com/docs/en/Datasheet/H77S.pdf, visited on 07.02.2024.

[49] *Titanium Grade2 Datasheet*, https://aerospacemetals.com/wp-content/uploads/2023/07/Titanium-Grade-2-Data-Sheet.pdf, visited on 25.03.2024.

[50] *Präzisions Glas Optik GmbH,N-BK7 glass properties*, https://www.pgo-online.com/intl/BK7.html, visited on 09.02.2024.

[51] S. Akterian, "Evaluating the vapour evaporation from the surface of pure organic solvents and their mixtures", 2018.

[52] K. L. M. Antonio Pizzi, ed., *Handbook of Adhesive Technology, Revised and Expanded*, 2nd edition, CRC Press, 2003 1024, ISBN: ISBN 0-8247-0986-1.

[53] N. Sajdera, *Surface tension*, Metal Finishing **105** (2007) 528.

[54] P. G. de Gennes, *Wetting: statics and dynamics*, Rev. Mod. Phys. **57** (3 1985) 827.

[55] *Relyon, Increased surface energy of glass*, https://www.relyon-plasma.com/inorganic-materials/?lang=en, visited on 25.03.2024.

[56] L. F. Raul A. Sadir Adriano Villarmosa, ed., *Clean Room Technology in ART Clinics*, 1st Edition, CRC Press, 2016, ISBN: 9781315372464.

[57] *Varian Vacuubrand MV2 Diaphragm Pump, M3H 2, Ultimate .6 Torr, KF16 inlet, 110-120 VAC 949-9451*, https://www.idealvac.com/files/manuals/Vacuubrand-MD4-MV2_Manual_2a.pdf, visited on 07.02.2024.

[58] *Technon syringe needle*, https://www.pkelektronik.com/techcon-dosiernadeln-te721050pk-groesse-21-lila-12-7-mm-50-stueck.html, visited on 07.02.2024.

[59] *Thorlabs LF6*, https://www.thorlabs.com/thorproduct.cfm?partnumber=LF6D, visited on 07.02.2024.

[60] S. Gerland and A. Raatz, *Adhesive Bonding of an Aluminum Alloy with and without an Oxide Layer in Atmospheres with Different Oxygen Contents*, Applied Sciences **13** (2023), ISSN: 2076-3417.

[61] *Reylon plasma PiezoBrush PZ3*, https://www.relyon-plasma.com/piezobrush-pz3/, visited on 07.02.2024.

[62] *Memmert UF260plus oven*, https://www.memmert.com/de/produkte/waerme-trockenschraenke/universalschrank/UF260plus/, visited on 08.02.2024.

[63] R. Stevens, *Measuring polarisation extinction ratio for optical fibres and components.*, (2003).

[64] *Thorlabs, Photodiode Power Sensor S121C*, `https://www.thorlabs.com/newgrouppage9.cfm?objectgroup_id=3328&pn=S121C`, visited on 18.03.2024.

[65] T. F. Gallagher, L. M. Humphrey, R. M. Hill and S. A. Edelstein, *Resolution of* $|m_l|$ *and* $|m_j|$ *Levels in the Electric Field Ionization of Highly Excited d States of Na*, Phys. Rev. Lett. **37** (22 1976) 1465.

[66] M. Kaiser et al., *Cavity-driven Rabi oscillations between Rydberg states of atoms trapped on a superconducting atom chip*, Phys. Rev. Res. **4** (1 2022) 013207.

[67] A. Gürtler and W. van der Zande, *l-state selective field ionization of rubidium Rydberg states*, Physics Letters A **324** (2004) 315, ISSN: 0375-9601.

[68] *Gerthsen Physik*, 25th edition, Springer Spektrum, 2015, ISBN: 978-3-662-45976-8.

[69] M. Mack et al., *Measurement of absolute transition frequencies of* ^{87}Rb *to nS and nD Rydberg states by means of electromagnetically induced transparency*, Phys. Rev. A **83** (5 2011) 052515.

[70] *Kimball Physics, 8.00" groove grabbers*, `https://www.kimballphysics.com/product/mcf800-grvgrb-c01/`, visited on 30.03.2024.

[71] *Allectra, Kapton wire with OD 1.4 mm and conductor 1.3 mm*, `https://shop.allectra.com/products/311-kap-130-5m`, visited on 30.03.2024.

[72] *Allectra, BNC feedthrough*, `https://shop.allectra.com/products/241-BNC-C40`, visited on 30.03.2024.

[73] *Allectra, Power push on connectors*, `https://shop.allectra.com/products/360-ppo-24`, visited on 30.03.2024.

[74] *Hamamatsu, Multi channel plate*, `https://www.hamamatsu.com/jp/en/product/optical-sensors/electron_ion-sensor/mcp/circular_fast-time-response_compact_demountable/F4655-10.html`, visited on 30.03.2024.

[75] T. Pyragius, *Developing and building an absorption imaging system for Ultracold Atoms*, 2012.

[76] H. Busche, *Efficient loading of a magneto-optical trap for experiments with dense ultracold Rydberg gases*, University Heidelberg, 2011.

[77] *Excelitas pco.pixelfly camera*, `https://www.excelitas.com/product/pcopixelfly-14-usb`, visited on 19.02.2024.

[78] *Thorlabs, polarization maintaining single mode fibre, 780nm*, `https://www.thorlabs.com/thorproduct.cfm?partnumber=P3-780PM-FC-10`, visited on 18.03.2024.

[79] *Thorlabs, Achromatic doublet,f=100nm ARC 650-1050nm*, `https://www.thorlabs.com/thorproduct.cfm?partnumber=AC508-100-B`, visited on 18.03.2024.

[80] D. Meschede, ed., *Optik,Licht und Laser*, Vieweg+Teubner, 2008, ISBN: 978-3-8351-0143-2.

[81] *ThorLabs, PM780-HP Datasheet*, https://www.thorlabs.com/drawings/f2bf68a928a1f71f-3E70C377-EBB1-BEC0-29BB9DD158AE8967/P3-780PM-FC-10-AutoCADPDF.pdf, visited on 28.03.2024.

[82] *Lens-Optics, W4Z40-780 Quarterwaveplate*, https://www.lens-optics.de/waveplates/, visited on 18.03.2024.

[83] *Thorlabs, Achromatic doublet,f=300nm ARC 650-1050nm*, https://www.thorlabs.com/thorProduct.cfm?partnumber=AC508-300-B&pn=AC508-300-B, visited on 18.03.2024.

[84] *Thorlabs, Achromatic doublet,f=150nm ARC 650-1050nm*, https://www.thorlabs.com/thorproduct.cfm?partnumber=AC508-150-B, visited on 18.03.2024.

[85] *Thorlabs, Achromatic doublet,f=60nm ARC 650-1050nm*, https://www.thorlabs.com/thorproduct.cfm?partnumber=AC254-060-B-ML, visited on 18.03.2024.

[86] *Thorlabs, Achromatic doublet,f=250nm ARC 650-1050nm*, https://www.thorlabs.com/thorProduct.cfm?partnumber=AC508-250-B&pn=AC508-250-B, visited on 18.03.2024.

[87] *Thorlabs, Achromatic doublet,f=100nm ARC 650-1050nm*, https://www.thorlabs.com/thorproduct.cfm?partnumber=AC254-100-B-ML, visited on 18.03.2024.

[88] *Kerafol KP12 Wärmeleitpaste 10 W/mK*, https://www.conrad.de/de/p/kerafol-kp12-0-5-kg-waermeleitpaste-10-w-mk-500-g-temperatur-max-150-c-1509024.html, visited on 23.03.2024.

[89] T. M. Brzozowski, M. Maczynska, M. Zawada, J. Zachorowski and W. Gawlik, *Time-of-flight measurement of the temperature of cold atoms for short trap-probe beam distances*, Journal of Optics B: Quantum and Semiclassical Optics **4** (2002) 62.

[90] G. Reinaudi, T. Lahaye, Z. Wang and D. Guéry-Odelin, *Strong saturation absorption imaging of dense clouds of ultracold atoms*, Opt. Lett. **32** (2007) 3143.

[91] D. Frese, *Bose-Einstein Condensation of Rubidium: Towards Ultracold Binary Bosonic Mixtures*, University Bonn, 2005.

[92] M. C. Ringler, *Aufbau und Charakterisierung einer Magnetfalle zum Speichern und Kühlen verdünnter atomarer Gase*, University Bonn, 2003.

[93] S. Germer, *Frequency stabilization of a laser and a high resolution optical setup for excitation of ultracold Ryderberg atoms*, University Bonn, 2023.

[94] V. Mauth, *Realization of a Rb87 magneto-optical trap*, University Bonn, 2023.

[95] J. Gamper, *Frequenzstabilisierung zur Laserkühlung von Rubidium*, University Bonn, 2022.